

2010

# Silica nanosphere textured back reflectors for increased absorption in thin film amorphous silicon solar cells

Brian Wellington Lewis  
*Iowa State University*

Follow this and additional works at: <https://lib.dr.iastate.edu/etd>

 Part of the [Electrical and Computer Engineering Commons](#)

## Recommended Citation

Lewis, Brian Wellington, "Silica nanosphere textured back reflectors for increased absorption in thin film amorphous silicon solar cells" (2010). *Graduate Theses and Dissertations*. 11466.  
<https://lib.dr.iastate.edu/etd/11466>

This Thesis is brought to you for free and open access by the Iowa State University Capstones, Theses and Dissertations at Iowa State University Digital Repository. It has been accepted for inclusion in Graduate Theses and Dissertations by an authorized administrator of Iowa State University Digital Repository. For more information, please contact [digirep@iastate.edu](mailto:digirep@iastate.edu).

**Silica nanosphere textured back reflectors for increased absorption in thin film  
amorphous silicon solar cells**

by

**Brian Wellington Lewis**

A thesis submitted to the graduate faculty

In partial fulfillment of the requirements for the degree of

**MASTER OF SCIENCE**

Major: Electrical Engineering

Program of Study Committee:  
Vikram Dalal, Co-Major Professor  
Rana Biswas, Co-Major Professor  
Joseph Shinar

Iowa State University

Ames, Iowa

2010

Copyright © Brian Wellington Lewis, 2010. All rights reserved.

## TABLE OF CONTENTS

LIST OF FIGURES.....	iv
LIST OF TABLES.....	vi
ABSTRACT.....	vii
CHAPTER 1. INTRODUCTION.....	1
1.1 Background.....	1
1.2 Structure of a Thin-Film Solar Cell.....	2
1.3 Absorption of Photons in Thin-Film Solar Cells.....	6
1.4 Use of Back Reflectors for Enhanced Path length and Photon Absorption.....	9
1.5 Literature Review.....	13
1.5.1 Textured Zinc Oxide.....	13
1.5.2 Photonic Structures.....	16
1.5.3 PEN Substrates and Nanoimprinting.....	18
1.5.4 Tandem Thin Film Solar Cells.....	19
1.5.6 Deposition of Monolayers of Nanospheres.....	20
1.5.6.1 Spin Coating Methods.....	20
1.5.6.2 Langmuir-Blodgett Methods.....	21
1.5.6.3 Dip-Coating Methods.....	21
2. METHODOLOGY AND PROCEDURES.....	23
2.1 Silica Nanosphere Back-Reflector Substrate Fabrication.....	23
2.1.1 Substrate Preparation.....	23
2.1.2 Colloid Preparation.....	24
2.1.3 Silica Nanosphere Deposition.....	25
2.1.4 Substrate Anneal.....	28
2.1.5 Ag Deposition.....	28
2.1.6 ZnO:Al Deposition.....	29
2.2 Solar Cell Deposition.....	30
2.2.1 a-si:H Cell Fabrication.....	30

2.2.3 ITO Deposition .....	32
CHAPTER 3. CHARACTERIZATION.....	33
3.1 Substrate Characterization .....	33
3.1.1 Scanning Electron Microscopy (SEM) .....	33
3.1.2 Spectroscopy Measurements .....	34
3.2 Solar Cell Device Characterization .....	35
3.2.1 I-V Measurement .....	35
3.2.3 Quantum Efficiency Measurement.....	36
CHAPTER 4. RESULTS AND DISCUSSION.....	39
4.1 Nanosphere Substrates.....	39
4.1.1 Dip-Coating Apparatus.....	39
4.1.2 Colloid Composition.....	40
4.1.3 Substrate Characteristics .....	41
4.2 Solar Cell Devices .....	43
4.2.1 a-Si:H Devices.....	43
4.2.2 nc-Si:H Devices.....	48
CHAPTER 5. CONCLUSIONS AND FUTURE WORK .....	49
APPENDIX: DIP-COATER ARDUINO CODE .....	50
BIBLOGRAPHY .....	52
ACKNOWLEDGEMENTS.....	55

## LIST OF FIGURES

Figure 1.1 – Representation of an n-i-p a-Si:H solar cell.....	3
Figure 1.2 – Absorption of incoming photons and ehp generation.....	4
Figure 1.3 – Energy band diagram of a solar cell showing an absorbed incoming photon, generated ehp, and electron and hole collected as current at the top and bottom contacts. Potential energy is shown on the y-axis and position on the x-axis.....	5
Figure 1.4 – Optical absorption of different types of Si.....	6
Figure 1.5 – Effect of the incident angle on the photon path length.....	7
Figure 1.6 – Effect of spectral back reflector on photon path length.....	8
Figure 1.7 – Solar Spectrum shown at AM0 (extraterrestrial) and AM1.5 (Earth's Surface).....	8
Figure 1.8 – Diffuse back reflector showing increased path length through a material.....	9
Figure 1.9 – Total internal reflection and absorption of a photon in a solar cell.....	11
Figure 1.10 – Diffuse Transmission (Haze) as a function of wavelength for ZnO films etched in dilute HCl for varying etch times.....	14
Figure 1.11 – AFM silver surfaces deposited on ZnO etched with increasing (from a to f) etch time. The roughness is stated in RMS terms.....	15
Figure 1.12 – 2-D Photonic Crystal with Cr/Ag/ZnO layers deposited on top of a Si substrate.....	16
Figure 1.13 – Simulation of absorption of solar cells with different types of back reflectors.....	17
Figure 1.14 – Simulation and device structure of a triangular lattice of nanocones.....	17
Figure 1.15 – Device structure of a PEN/Ag/ZnO tandem a-si:H/ $\mu$ c-Si:H solar cell.....	18
Figure 1.16 – Quantum Efficiency of Unisolar's Triple Junction Si:H/a-SiGe:H/ncSi:H solar cell.....	19
Figure 1.17 – The effect of RIE times on a monolayer of PS spheres. The scale bar is 1 $\mu$ m.....	21

Figure 1.18 – Visual Representation of a) Dip-Coating method and b) Langmuir-Blodgett method.....	22
Figure 2.1 – Highly simplified schematics of the dip coating apparatus.....	25
Figure 2.2 – SEM images showing 500nm nanospheres dip-coated at periods of 50ms, 100ms, 200ms, and 400ms between step motor advances from top left to bottom right.....	27
Figure 2.3 – Simplified schematic of a PECVD Reactor.....	31
Figure 3.1 – Sample IV Curve of a Solar Cell.....	35
Figure 3.2 – Diagram of the Quantum Efficiency Measurement System.....	37
Figure 4.1 – Periodic bunching of monolayer due to imperfections in the dip-coating apparatus.....	39
Figure 4.2 – High magnification of periodic bunching.....	40
Figure 4.3 – Monolayer of nanosphere particles deposited on glass (left) and stainless steel (right) with a layer of Ag deposited on top of the nanospheres.....	41
Figure 4.4 – Diffuse reflection of substrates after Ag deposition.....	42
Figure 4.5 – Diffuse reflection of substrates after ZnO:Al deposition.....	42
Figure 4.6 – Total reflection of substrates after Ag and ZnO:Al depositions.....	43
Figure 4.7 – SEM image of the top surface of the solar cell device.....	44
Figure 4.8 – Normalized EQE measurement of sample 2-13182.....	46
Figure 4.9 – EQE enhancement of sample 2-13182.....	46
Figure 4.10 – IV measurement of sample 2-13182.....	47
Figure 4.11 – SEM image of nc-Si:H device peeling off at periodic bunching boundaries..	48

**LIST OF TABLES**

Table 1.1 – Table of critical angles by photon wavelength.....	12
Table 2.1 – Properties of the Silica Nanospheres.....	24
Table 2.2 – Optimal Colloid Solution.....	26
Table 2.3 – ZnO:Al Deposition Parameters.....	30
Table 2.4 – ITO Deposition Parameters.....	32
Table 4.1 – Summary of device characteristics.....	45

## ABSTRACT

Absorption of long-wavelength photons in thin-film hydrogenated amorphous silicon (a-Si:H) solar cells is inherently low due to an absorption layer thickness of 250-300nm and long absorption lengths for photons of wavelengths above 700nm. When used in a thin-film solar cell, back reflectors that exhibit diffuse reflection increase the probability of absorption by lengthening the path-lengths of photons. Ordered monolayers of silica nanospheres coated with a reflective surface were investigated for use as a diffuse back reflector.

A method for fabricating a monolayer of silica nanospheres was developed using a custom built dip-coating apparatus. Repeatable monolayers of 500nm nanospheres were fabricated on glass and stainless steel substrates. The monolayers were covered with a 200nm layer of silver (Ag) and a 200nm layer of aluminum-doped zinc oxide (ZnO:Al) to be used as a back-reflector in a-Si:H solar cells .

The back-reflector substrates were measured to have a much higher percentage of diffuse reflectance when compared to flat silver back-reflector substrates. Increases in long-wavelength absorption were observed by normalized external quantum efficiency (NEQE) measurements of the a-Si:H solar cells. Short circuit current density increases were seen in both I-V measurements under AM1.5 lighting as well as in NEQE measurements.

## CHAPTER 1. INTRODUCTION

### 1.1 Background

In 2008, the worldwide energy consumption was 474 exajoules ( $474 \times 10^{18}$  J) [1]. In the future, energy demands will drastically increase from current levels due to increasing demands from developing countries and an ever-increasing population. To meet future demands, drastic changes and additions to our current sources of energy must be made. These changes include developing technologies to increase the efficiency of solar power conversion, gas engines, the electrical grid, and many other energy processes. Currently, over 80% of the worldwide energy demands are met with oil, coal, and natural gas [1] while a very small percentage is supplied by renewable resources such as solar energy, wind energy, hydroelectric, and geothermal energy. To address global energy and environmental issues, renewable energy sources must become a larger part of the worldwide energy supply in the future.

Solar energy is a very attractive form of renewable energy. It has excellent applications in remote parts of the world where other forms of energy or a power grid are unavailable. Solar energy harvested using solar cells can be setup in configurations suitable for many different applications ranging from solar battery chargers to large arrays configured as power plants with capacities larger than 10 MW [2]. While there are many different types of materials and methods to produce solar cells, the most popular solar cells are based on crystalline Silicon (c-Si). Despite the high efficiencies attainable by these cells, their costs do not allow them to economically compete with energy produced with fossil fuels. C-Si-based solar cells require mono-crystalline Si

wafers, a main component in costly computer microchips, memory, and other various microelectronic devices. The cost of high-purity monocrystalline Si wafers necessary for computer chip manufacturing, and therefore available for solar cell manufacturing, limits the cost effectiveness of crystalline solar cells.

Typically, Si wafers used in computer chip manufacturing processes are 200-300 $\mu\text{m}$  thick. Consequentially, c-Si solar cells are approximately 200-300 $\mu\text{m}$  thick. However, using different techniques, Si-based solar cells can be fabricated to be as thin as 0.5 $\mu\text{m}$ . These solar cells are in the class of thin-film solar cells. This class of Si based cells include hydrogenated amorphous silicon (a-Si:H) and hydrogenated nano-crystalline Silicon (nc-Si:H) solar cells. With the reduced amount of Si used in the latter comes a reduced cost of production. However, thin-film solar cells are not as efficient as crystalline solar cells due to difficulties in absorbing long wavelength photons as well as material defects. Improving the efficiency of thin-film solar cells is necessary to drive down the cost enough to compete with fossil fuel derived energy.

## 1.2 Structure of a Thin-Film Solar Cell

Thin-film solar cells are usually created in one of two configurations, n-i-p or p-i-n structures. These configurations are referencing regions of n-type (n), p-type (p), and intrinsic (i) Si or any other semiconductors being used. An n-type Si region is a region embedded or “doped” with donor atoms or “dopants” that contain one more valence electron than Si. Common n-type dopants for Si include phosphorus, arsenic, and antimony. As n-type dopants donate an extra electron to Si, p-type dopants accept an

extra electron from Si. Common p-type dopants include boron and aluminum. The structure shown in Figure 1.1 is that of a p-i-n solar cell. In addition to the various layers of Si, the solar cell is built on a substrate that typically serves as a back contact and reflector. The substrate is most commonly composed of stainless steel or glass with a conductive layer coated between the glass and n layer, but can also be made of flexible polymers. On the top of the solar cell, there is a top contact, which in conjunction with the back contact allows for current to be collected from the solar cell. The top contact must be conductive and transparent. Popular choices for top contacts are the transparent conducting oxides (TCO) Indium Tin Oxide (ITO) and Zinc Oxide (ZnO). ITO is commonly used as a top contact for its ability to act as an anti-reflection coating, trapping any light inside the solar cell that is incident on the ITO/p-type layer interface at a sufficient angle.

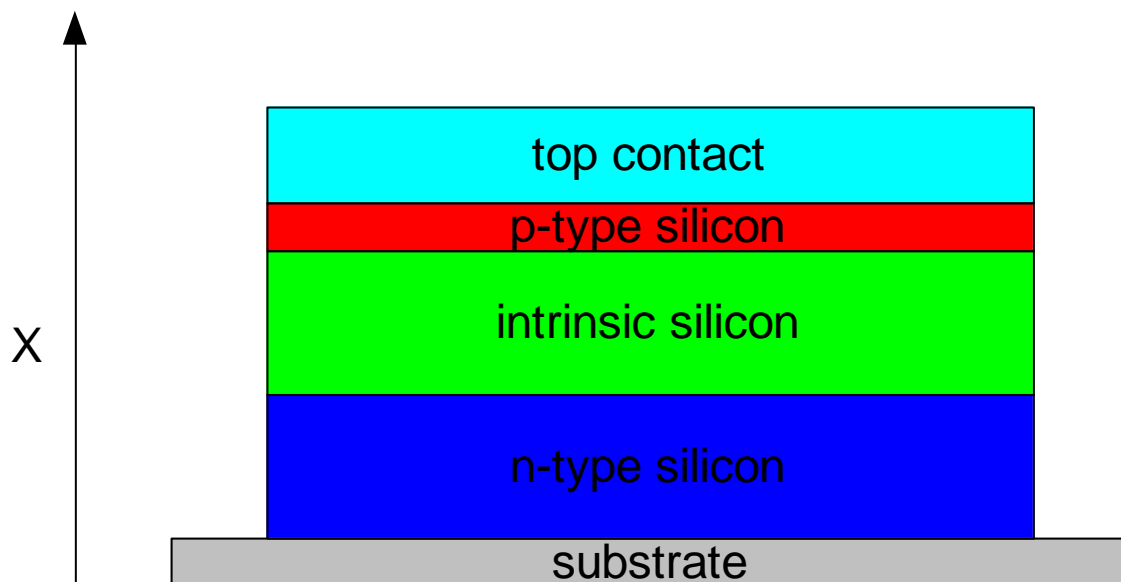


Figure 1.1 – Representation of an n-i-p a-Si:H solar cell

As incoming light enters the cell, photons pass through the transparent top contact and the thin p-type region into the intrinsic layer where the light is absorbed. Each photon absorbed creates an electron-hole pair (ehp). The electron ( $e^-$ ) and hole ( $h^+$ ) then travel to separate ends of the solar cell. The process of ehp generating by light absorption, is shown in Figure 1.2.

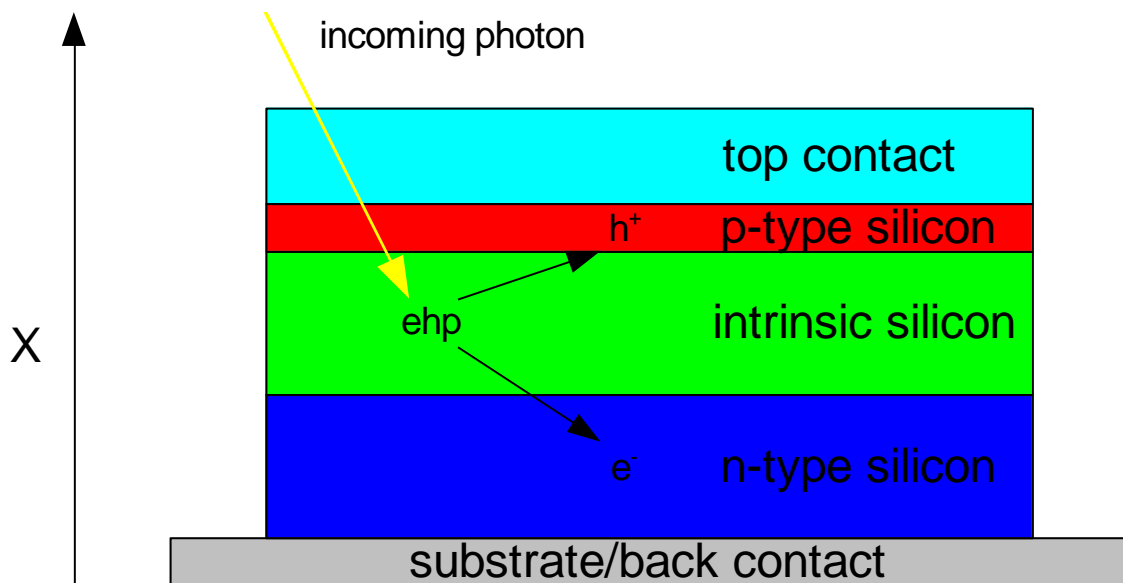


Figure 1.2 – Absorption of incoming photons and ehp generation

After the ehp is created, the electron is swept away to the n-type region and the hole is swept away to the p-type region. This occurs due to an internal electric field, which is a result of the differences in Fermi-levels ( $E_f$ ) of the p-type and n-type regions. Figure 1.3 shows the electric field forcing the electron and hole to separate and then be collected at separate ends of the solar cell.

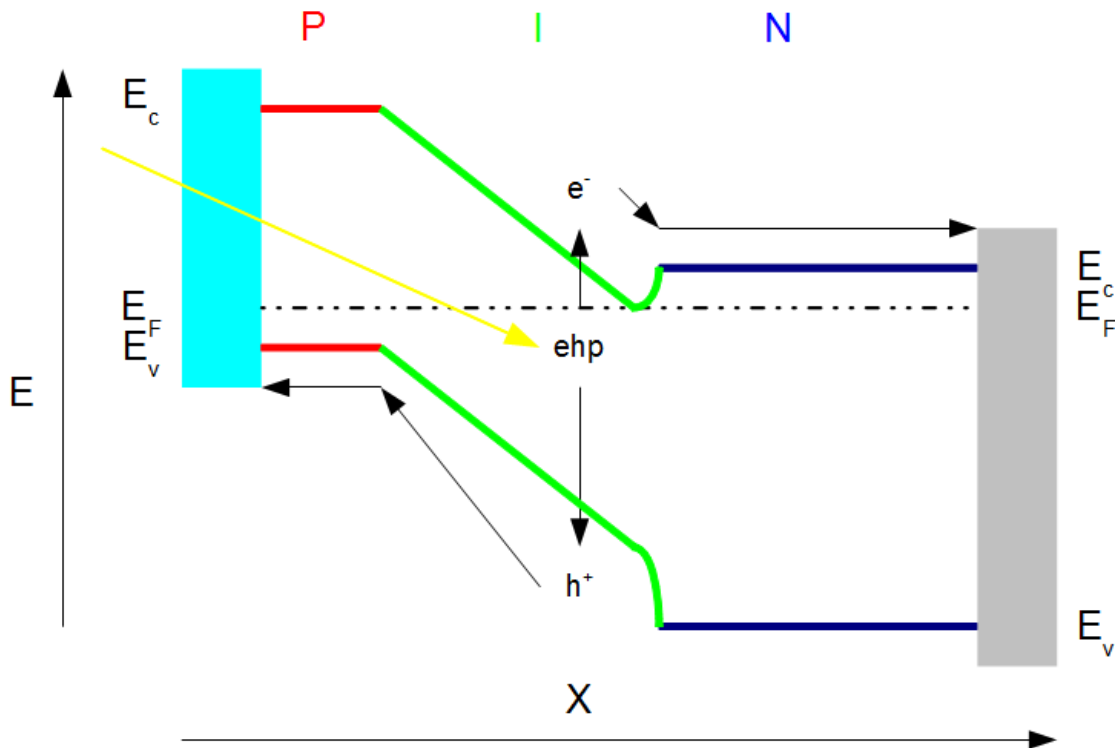


Figure 1.3 – Energy band diagram of a solar cell showing an absorbed incoming photon, generated ehp, and electron and hole collected as current at the top and bottom contacts. Potential energy is shown on the y-axis and position on the x-axis.

As more incident photons pass through the top contact of the solar cell, more photons will be absorbed in the intrinsic layer (green) and electron-hole pairs will be generated. Each electron and hole will be transported to the conduction band ( $E_c$ ) and valence band ( $E_v$ ) respectively, as shown in Figure 1.3. Every electron and hole collected at the back contact and top contact, respectively, will contribute to the photo-generated current. This is the general principle behind a solar cell.

### 1.3 Absorption of Photons in Thin-Film Solar Cells

The absorption of photons is what generates current in solar cells. How well the intrinsic layer absorbs photons at the wavelengths of light that enter it governs how many ehrs are generated. This trait is measured by the absorption coefficient ( $\alpha$ ). A larger absorption coefficient results in enhanced absorption for a given film thickness. For Si, the absorption coefficient varies drastically within photon energies within the spectrum of normal incident light. Absorption coefficients for different types of Si are shown in Figure 1.4.

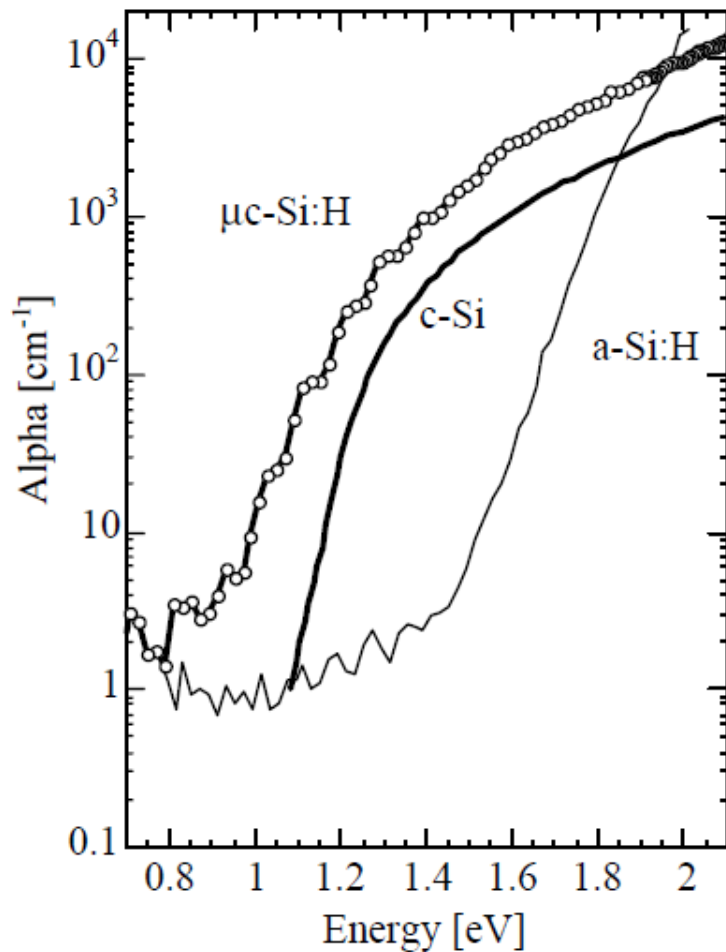


Figure 1.4 – Optical absorption of different types of Si [3]

The probability of absorbing a photon and creating an ehp is related to the path length ( $d$ ) the photon travels through the material and the absorption coefficient of the material at a given wavelength, as shown by Equation 1.1 [4].

$$P(\lambda) = 1 - \exp(-d * \alpha(\lambda)) \quad (1.1)$$

The path length can vary due to the photons' incident angle. This point is illustrated in Figure 1.5. By changing the incident angle from  $0^\circ$  to  $\theta^\circ$ , the path length  $d$  changes from the thickness of the material ( $t$ ) to  $t / \cos(\theta)$ .

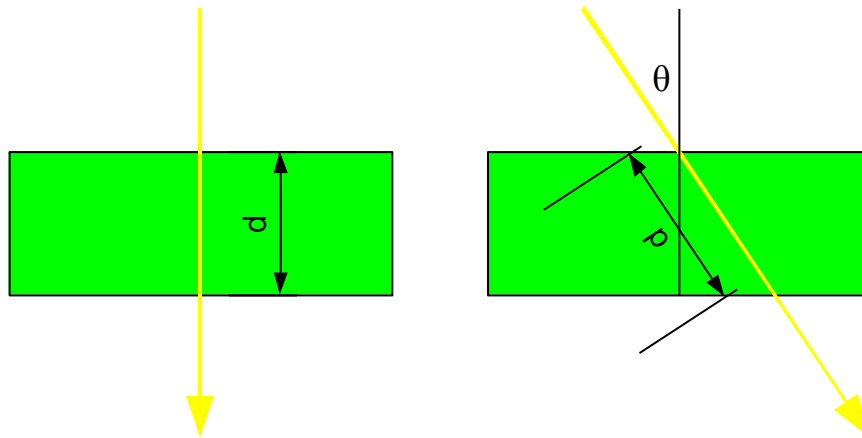


Figure 1.5 – Effect of the incident angle on the photon path length

When an ideal spectral back reflector is used as a back contact, such as silver which has  $>90\%$  reflection for all visible wavelengths [5], the increase is doubled as shown in Figure 1.6.

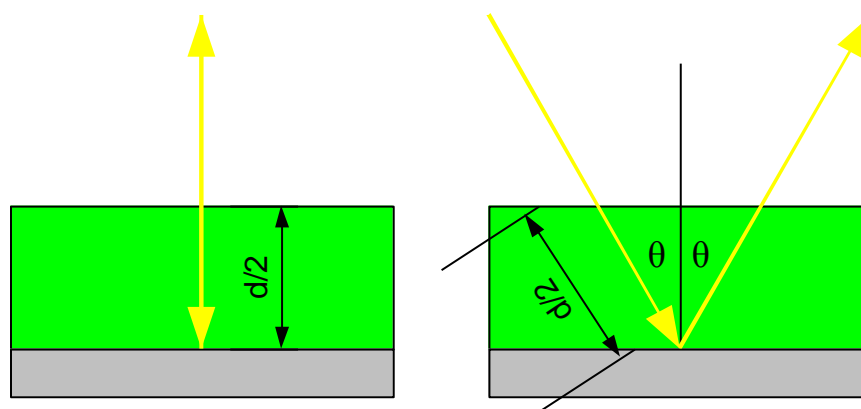


Figure 1.6 – Effect of spectral back reflector on photon path length

As the thickness increases, the probability of collecting long-wavelength photons increases. However because thin-film solar cells are limited in their thickness due to low hole lifetimes, thin-film solar cells absorb poorly at longer wavelength. As shown in Figure 1.7, the solar spectrum extends far past the optimal absorption range for a-Si:H (<750nm), c-Si (<1100 nm), or even micro-crystalline Si (<1200nm).

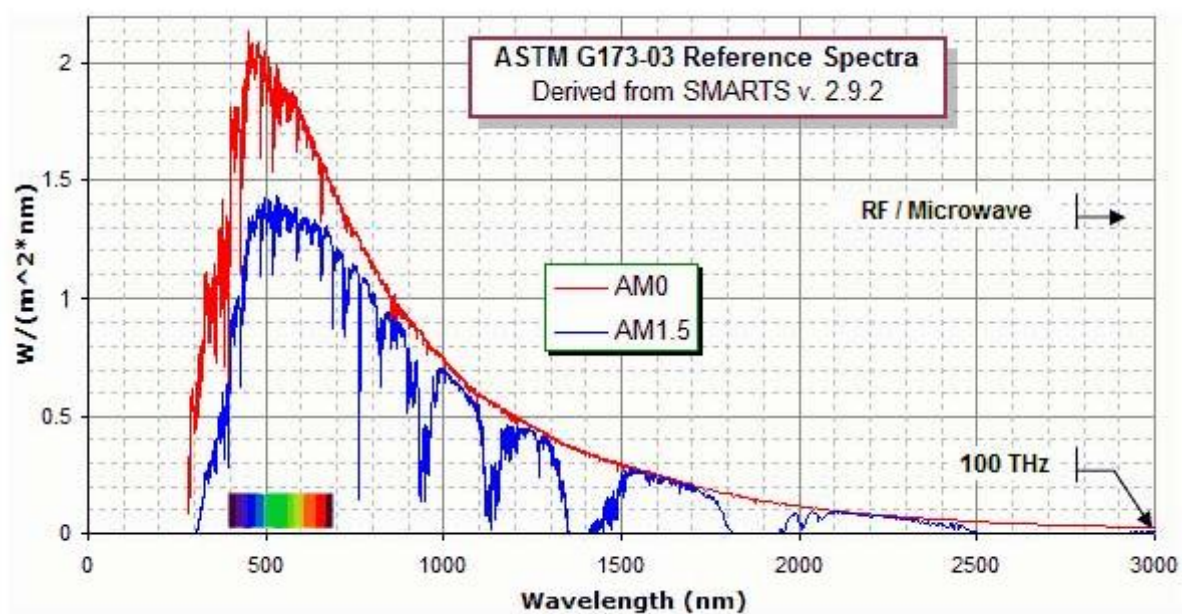


Figure 1.7 – Solar Spectrum shown at AM0 (extraterrestrial) and AM1.5 (Earth's Surface) [6]

## 1.4 Use of Back Reflectors for Enhanced Path length and Photon Absorption

As previously mentioned above, a very effective way of increasing the path length of photons inside a solar cell is to use a back-reflector as the substrate of a p-i-n solar cell. A back-reflector with a perfect spectral reflection, with the incident light normal to the cell, will double the path length of photons when compared to a non-reflecting back contact. This concept was shown in Figure 1.6. By using a back reflector that exhibits diffuse reflection properties instead, the incoming photons can be reflected at a much higher angle in reference to normal, as shown in Figure 1.8. This increases the path length through the material by a much larger amount than the reflectors shown earlier. Hence, diffuse reflection is a highly sought characteristic in back reflectors for use in thin-film solar cells.

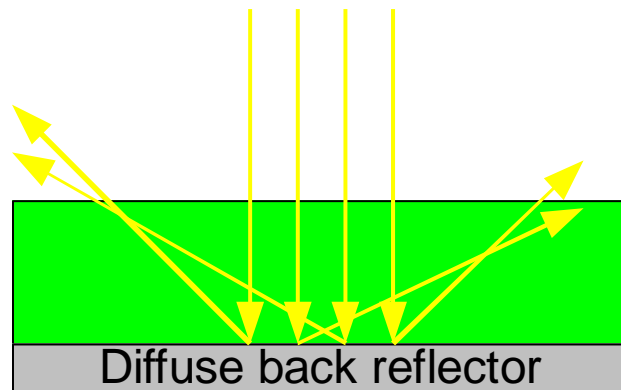


Figure 1.8 – Diffuse back reflector showing increased path length through a material

Applying the principal of using a diffuse back reflector to increase path length in a solar cell is achieved by placing the back reflector below the n-type region in an n-i-p solar cell. This back reflector reflects any photons that are not absorbed in the thin solar cell back through the cell at an increased angle (for a diffuse back reflector). The main benefit of using a diffuse back reflector in a thin-film solar cell is the increased absorption of long-wavelength (low-energy) photons that inherently have a low absorption coefficient in Si (Figure 1.4). Also, if the angle of reflectance that the reflector produces is large enough, total internal reflection can be achieved, as shown in Figure 1.9. Total internal reflection occurs when the angle incident on the top contact,  $\theta$ , is larger than the critical angle as defined by Snell's Law (Equation 1.2) [7].

$$\theta_{critical} = \arcsin\left(\frac{n_{top\ contact}}{n_{p-type\ silicon}}\right) \quad (1.2)$$

Total internal reflection ensures that a photon gets absorbed as its path length approaches infinity. In the case of the described solar cell, the critical angle is dependent on the ratio of refractive indices of the top contact material and the p-type Si layer.

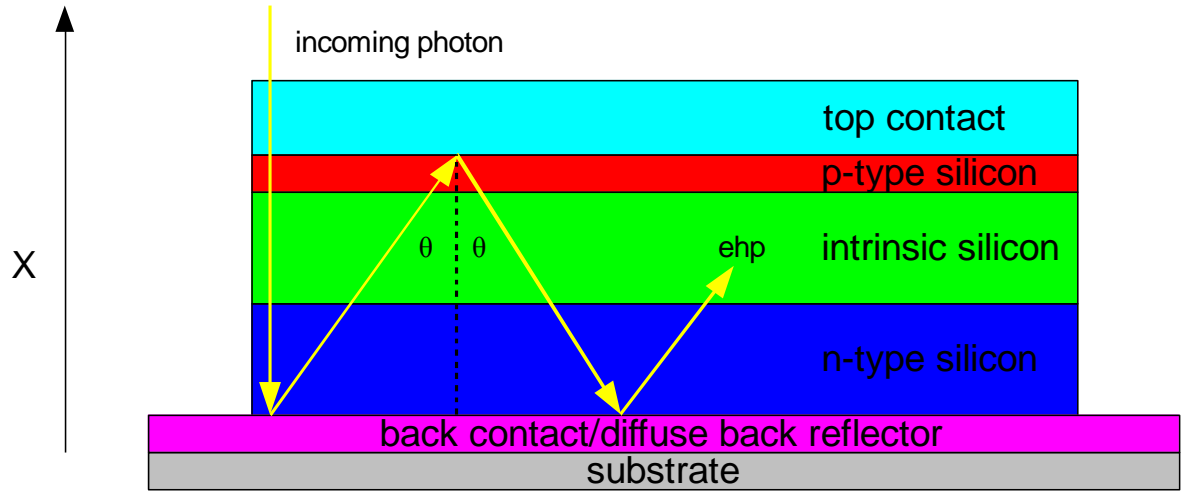


Figure 1.9 – Total internal reflection and absorption of a photon in a solar cell

It becomes apparent from Equation 1.2 that a top contact of lower refractive index gives a smaller critical angle and a larger chance of total internal reflection. When a top contact is engineered for this use, it is many times referred as an anti-reflection coating. The refractive index of amorphous Si is given by Equation 1.3 [8].

$$n_{\text{amorphous Si}} = \frac{2 \cdot 10^5}{\lambda^2} + 2.6 \quad (1.3)$$

If a refractive index of 2.06 is used for ITO [9] and Equation 1.3 is used for the refractive index of Si for the p-type region, the critical angle can be calculated for many wavelengths of light, shown in Table 1.1.

Wavelength [nm]	Refractive Index of a-Si	Critical Angle [degrees]
350	3.42	37.08
400	3.23	39.70
450	3.09	41.75
500	3.00	43.37
550	2.93	44.66
600	2.88	45.71
650	2.84	46.57
700	2.80	47.28
750	2.78	47.87
800	2.76	48.36
850	2.74	48.79
900	2.72	49.15
950	2.71	49.46
1000	2.70	49.73
1050	2.69	49.96
1100	2.68	50.17
1150	2.68	50.35

Table 1.1 – Table of critical angles by photon wavelength

It is apparent that as the wavelength increases, it becomes more difficult to achieve total internal reflection. Combining this with the fact that the absorption coefficient of Si decreases rapidly at long wavelengths, it becomes apparent that having a diffuse back reflector can greatly increase absorption of longer wavelength photons. Increased long wavelength absorption will increase current densities and contribute to higher efficiency thin film solar cells.

## 1.5 Literature Review

The absorption of all wavelengths of the solar spectrum by thin film solar cells is an ongoing problem. There are many different types of back reflectors that have been used and are being manufactured today to help solve this problem. There are also other methods to trap light in thin film solar cells. A few of these methods involve photonic structures, multiple layers, unique substrates, and novel structures such as nanowires and nanodots. What all of these methods have in common, is that they are designed to enable the solar cells to more efficiently absorb the entire spectrum of the incident light. In this section, an overview of some of the current techniques of increasing absorption as well as a few of the more revolutionary approaches to thin film solar cell design will be covered. The fabrication of monolayers of nanosphere particles for use as back reflectors will also be covered as this is the basis of much of the research done on this project.

### 1.5.1 Textured Zinc Oxide

Textured zinc oxide (ZnO) superstrates are a very popular choice for increased light enhancement due to the availability of equipment needed to produce the films and the generally low cost of manufacturing. ZnO superstrates are designed to be diffuse transmitters contributing to longer path lengths and better absorption of long wavelength photons. ZnO, fabricated on glass, is used as the first layer of a superstrate cell; it is followed by the Si solar cell layers. A highly transmissive and conductive layer, such as ZnO is used.

The preparation of the superstrate involves depositing ZnO films via radio frequency (rf) or dc sputtering on a glass substrate [10]. This can be done at relatively low temperatures (<200 °C) and at moderate vacuum levels (5-10 mTorr). After a layer of ZnO is grown, it is etched in dilute HCl to produce the diffusely transmitting surface. The etch time of the ZnO film leads to different diffuse transmission (% Haze) characteristics as shown in Figure 1.10 [10].

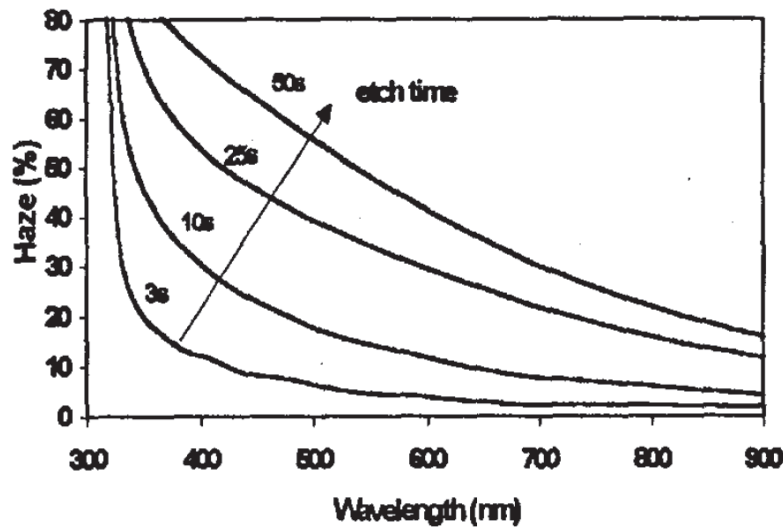


Figure 1.10 – Diffuse Transmission (Haze) as a function of wavelength for ZnO films etched in dilute HCl for varying etch times [11]

In the same way that the glass-ZnO superstrates helps diffract incoming light, Glass-ZnO-Ag substrates can be made to diffusely reflect light as a back reflector. Combining the texture of the ZnO with a highly reflective silver layer, results in a highly diffuse back reflector at a low cost. Substrates made using this method with different rms roughness due to different HCl etching times are shown in Figure 1.11.

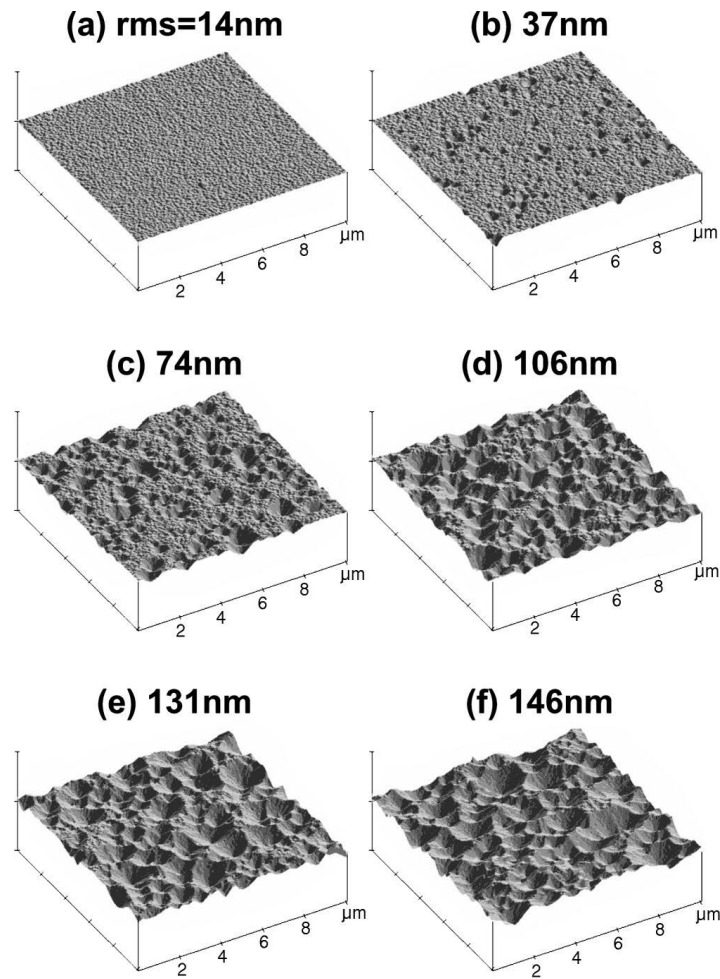


Figure 1.11 – AFM silver surfaces deposited on ZnO etched with increasing (from a to f) etch time. The roughness is stated in RMS terms. [10]

Solar cells made using this method have shown efficiencies of 9.2% for single layer a-Si:H, 10.1% for tandem a-Si:H/a-Si:H, and 11.1% for a-Si:H/ $\mu$ c-Si:H [10].

## 1.5.2 Photonic Structures

Photonic structures are periodic structures of nanometer scale that can show unique diffraction characteristics and can be tuned to provide a specific diffraction spectrum. Figure 1.12 shows a 2-D array or periodic 500nm holes etched into a Si wafer in a triangular lattice. This lattice, shown with a thin layer of Cr (5 nm), a layer of Ag (50nm), and a layer of ZnO (100nm) deposited on it, provides a diffusely reflecting surface for a thin film solar cell.

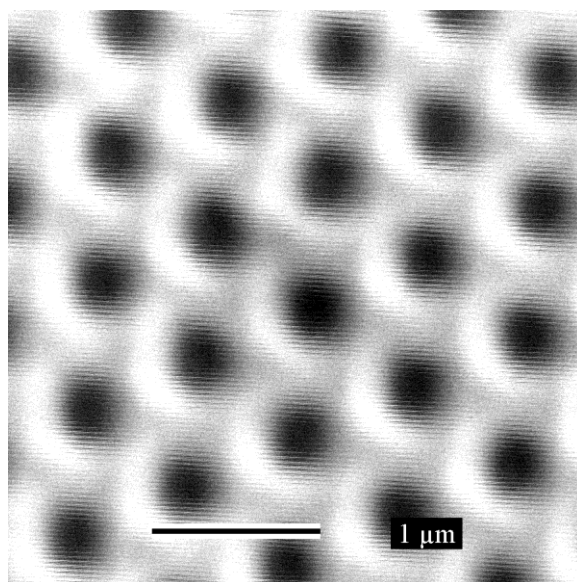


Figure 1.12 – 2-D Photonic Crystal with Cr/Ag/ZnO layers deposited on top of a Si substrate

The above design was used to fabricate an a-si:H solar cell with an intrinsic layer thickness of 250-300nm. An increase in photon absorption and current density of the solar cell of 7% was observed [12]. In Figure 1.13, the % absorption of the solar cell when compared to a flat Ag back reflector design and the theoretical limit of diffuse back reflectors of  $4n^2$  shows the photonic crystal design outperforming ideal diffuse reflectors at wavelengths  $> 740\text{nm}$ .

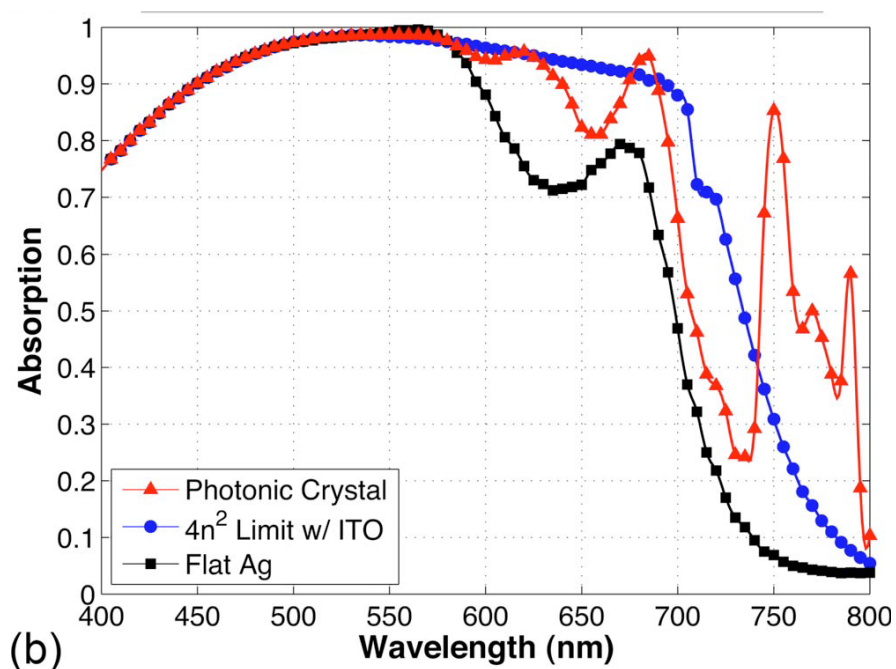


Figure 1.13 – Simulation of absorption of solar cells with different types of back reflectors

Another advantage of photonic structures is that they allow for diffraction resonances (standing waves) to be trapped and absorbed within the solar cell. Many types of photonic structures can be fabricated. A triangular cone lattice structure being investigated as a possible texture for a substrate is shown in Figure 1.14 [13].

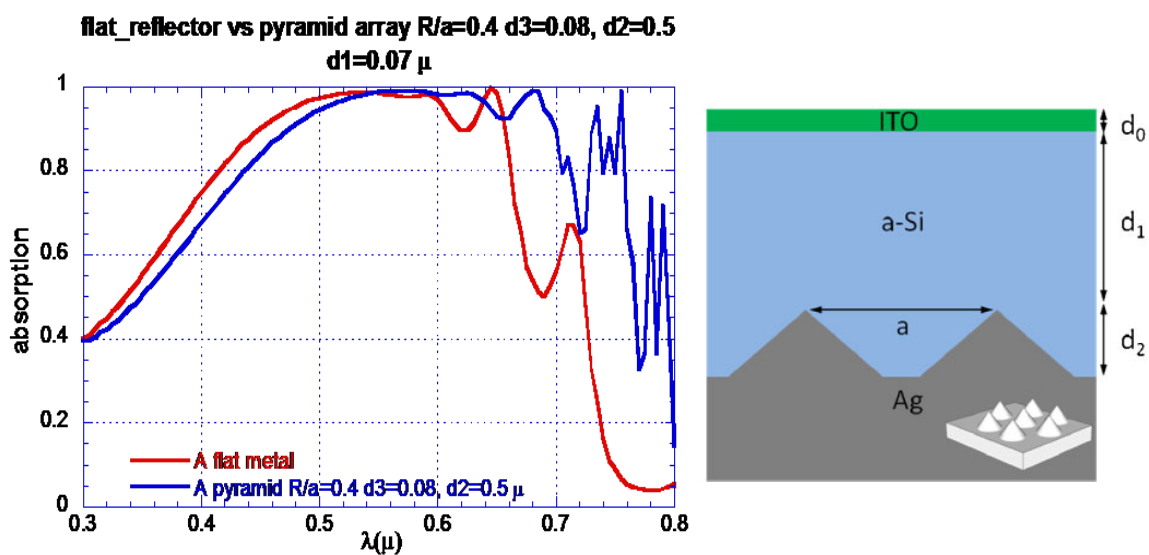


Figure 1.14 – Simulation and device structure of a triangular lattice of nanocones

As shown in the simulation in Figure 1.14, the nanocone array greatly outperforms a flat metal back reflector for wavelength  $> 650\text{nm}$ .

### 1.5.3 PEN Substrates and Nanoimprinting

Novel plastic substrates such as PEN (polyethylene naphthalate) have been used with the process of nanoimprinting to create flexible and textured substrates [14]. Nanoimprinting uses a hard mold to emboss the PEN substrates at a high temperature and leave an imprint of the mold embedded in the surface. The mold can be many different 2-D structures including photonic nanohole arrays or randomly textured surfaces [14]. a-Si:H solar cells built on textured PEN/Ag/ZnO structures have been shown to have stable efficiencies of over 8% while tandem a-si:H/ $\mu\text{c-Si:H}$  cells built on textured PEN/Ag/ZnO substrates have achieved efficiencies of over 10% [15]. Figure 1.15 shows the device structure of the mentioned tandem a-si:H/ $\mu\text{c-Si:H}$ .

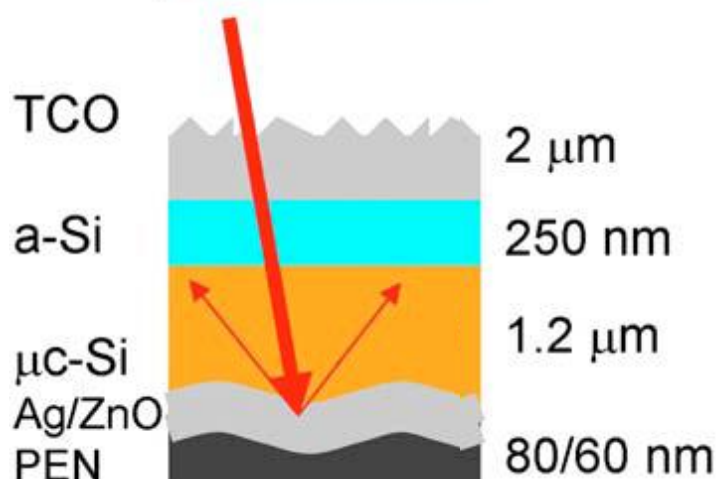


Figure 1.15 – Device structure of a PEN/Ag/ZnO tandem a-si:H/ $\mu\text{c-Si:H}$  solar cell

### 1.5.4 Tandem Thin Film Solar Cells

Tandem thin film solar cells have been shown to give great efficiencies. Combining layers of differing bandgaps that allow for optimal absorption of different wavelengths in one cell can allow for more complete absorption of the entire spectrum. However, the more complex structure of combining layers comes at an increased cost. An extreme case of a thin film tandem cell is Unisolar's 15.4% (initial efficiency) triple junction a-Si:H/a-SiGe:H/ncSi:H solar cell [16]. The quantum efficiency of the different layer and overall quantum efficiency are shown in Figure 1.16. Quantum efficiency is defined as the amount of photons absorbed and collected as current divided by the total amount of photons available at a given wavelength.

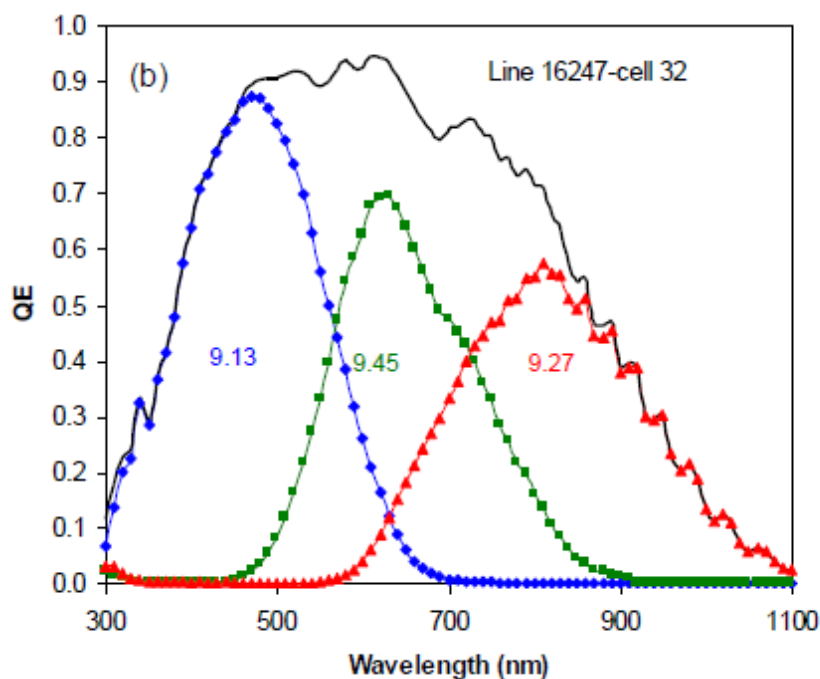


Figure 1.16 – Quantum Efficiency of Unisolar's Triple Junction Si:H/a-SiGe:H/ncSi:H solar cell

## 1.5.6 Deposition of Monolayers of Nanospheres

In this project, a textured substrate of a monolayer of nanosphere particles with silver and zinc oxide films was produced. Therefore, an overview of the various methods of producing monolayer arrays of nanospheres will be covered. There are three main types of nanosphere particles used in most monolayer constructions, titania ( $\text{TiO}_2$ ) spheres, silica ( $\text{SiO}_2$ ) spheres, and polystyrene (PS) spheres. These spheres sizes vary from a few nanometers to hundreds of microns in diameter. Due to the high melting point and availability of silica spheres, they were used in this project. However, methods for other types of nanospheres are covered.

### 1.5.6.1 Spin Coating Methods

Spin coating a monolayer of nanoparticles requires deposition at a controllable rate. The nanospheres are dispersed in a solution and a colloid is formed. The colloid is then dropped onto the surface of the substrate, which is spun to spread the colloidal solution across the substrate.

Researchers at Lawrence Livermore National Laboratory created a process of creating a monolayer of PS beads of 500nm diameter by using a carefully constructed colloid and different spin rates and times [17]. Their solution was comprised of 12.5% by volume Triton X-100 (a common surfactant) diluted with methanol 1:400 and 87.5% by volume 500nm diameter polystyrene beads. The solution was spun on a Si wafer that was cleaned with an RCA cleaning. The spin coating procedures were as follows:

1. 400 rpm for 10 seconds to spread the beads evenly
2. 800 rpm for 2 minutes to spin away excess bead solution

3. 1400 rpm for 10 seconds to spin off the excess material from the edges

This procedure produced a very uniform monolayer that was further etched using RIE O<sub>2</sub> plasmas to produce an array of smaller particles. They then used the monolayer of particles as a mask to produce nanowires in the Si wafer. Different RIE etching times produced spheres of different sizes as shown in Figure 1.17 [17].

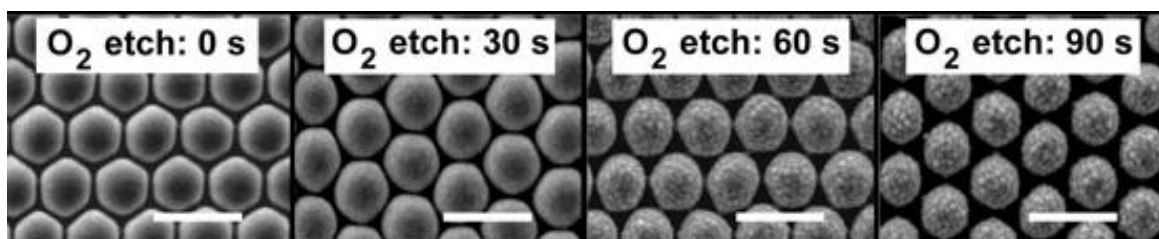


Figure 1.17 – The effect of RIE times on a monolayer of PS spheres. The scale bar is 1 $\mu$ m.

#### 1.5.6.2 Langmuir-Blodgett Methods

The Langmuir-Blodgett method of creating a monolayer of nanospheres involves the nanospheres being deposited between a layer of two dispersive liquids or a liquid and air. A monolayer forms at the liquid/oil and is transferred to a substrate as the substrate is pulled out of the liquid, or the liquid is evaporated. This is also a method that is transferrable to commercial products and processes such as roll to roll manufacturing.

#### 1.5.6.3 Dip-Coating Methods

A third method for producing monolayers is via a dip-coating. This is done by creating a colloidal dispersion of nanospheres and pulling the substrate through this dispersion. The substrate is pulled at a very slow rate (<10 $\mu$ m/sec) to deposit the spheres in a monolayer via capillary forces. The capillary forces create a monolayer when the thickness of the liquid approaches the thickness of the nanospheres. A visual

comparison of dip-coating versus the Langmuir-Blodgett method is shown in Figure 1.18 [18].

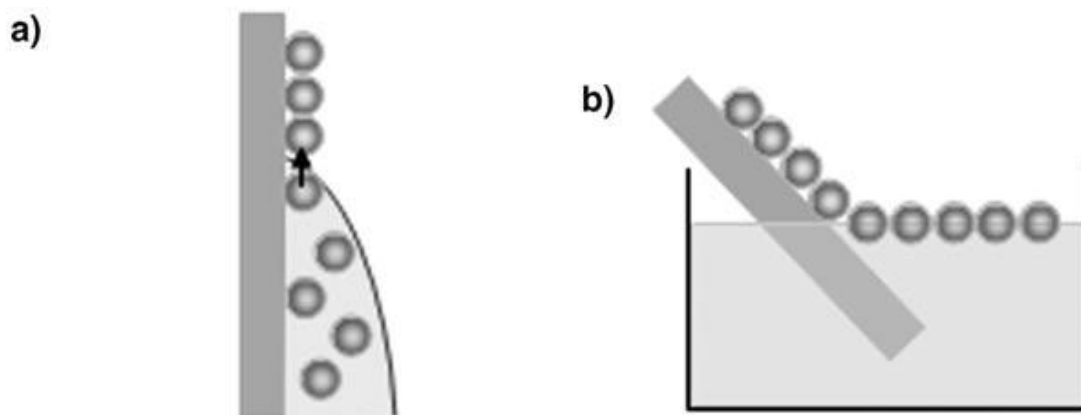


Figure 1.18 – Visual Representation of a) Dip-Coating method and b) Langmuir-Blodgett method

Dip-coating was chosen for use in this research as it is very applicable for roll to roll processing and can be done in a very cost effective way. Dip coating is, however, very sensitive to the speed the substrate is pulled out of the colloid and the composition of the colloid. A very slight change in the chemistry of the colloid can have an adverse effect on the quality of the monolayer.

## 2. METHODOLOGY AND PROCEDURES

Research was done on developing a dip-coating process for creating a reproducible monolayer of silica nanospheres on a substrate to be used as a back-reflector/contact in solar cells. This process begins with producing a colloidal solution of silica nanosphere. Next, the silica nanospheres are transferred to a substrate via dip-coating. This is followed with a high-temperature anneal to ensure that the liquid has been completely eliminated from the surface of the substrate; silver and zinc oxide layers are then deposited on the spheres to ensure a highly reflective and conductive back-reflector. Following fabrication of the back-reflector, an a-si:H or nc-Si:H solar cell is deposited using plasma enhanced chemical vapor deposition (PECVD). The following section will cover the methods to produce the substrates and solar cells

### 2.1 Silica Nanosphere Back-Reflector Substrate Fabrication

#### 2.1.1 Substrate Preparation

Various substrates were tested during this project with most development performed on pre-cleaned 1" x 3" microscope glass slides. This was done because of the availability and low cost of these substrates. During the development of the process, various defects were not an issue and were generally disregarded. Sandblasted microscope glass slides were also investigated as a possible substrate, but were decided against due to lower packing density of spheres on them. All solar cells were built on 2" x 2" stainless steel substrates which went through a rigorous cleaning routine to ensure

no defects due to particles on the surface of the substrates. The cleaning procedure is outlined below.

1. 15 minute boil in acetone
2. Rinse in methanol
3. 15 minute boil in 1:1:1 H<sub>2</sub>O<sub>2</sub>:H<sub>2</sub>O:NH<sub>4</sub>OH
4. 15 minute ultrasonication in methanol
5. Store in methanol

### 2.1.2 Colloid Preparation

The colloid was prepared by dispersing silica nanospheres in a mixture of alcohol, DI water, and Triton X-100 surfactant. The silica nanospheres were purchased from Fiber Optic Center Inc. The specifications of the spheres are listed in Table 2.1 [19].

Diameter	500nm
Density	1.8 grams/cc
Structure	Amorphous
Purity	>99.9%
Dielectric Constant	3.8
Refractive Index	1.38-1.46
Surface Area	2-6 m <sup>2</sup> /g
Melting Point	1840 °C
Softening Point	1600 °C

Table 2.1 – Properties of the Silica Nanospheres

The colloid was prepared by ultrasonating solutions of varying amounts of nanospheres, alcohol, water, and surfactant for a minimum of 30 minutes. After sonication, the colloid was allowed to cool to room temperature for 30 minutes.

### 2.1.3 Silica Nanosphere Deposition

The spheres were transferred to the surface of the substrate by dip-coating the substrates in the colloid. This was done by using a custom-made dip-coating machine as shown in a highly simplified version in Figure 2.1.

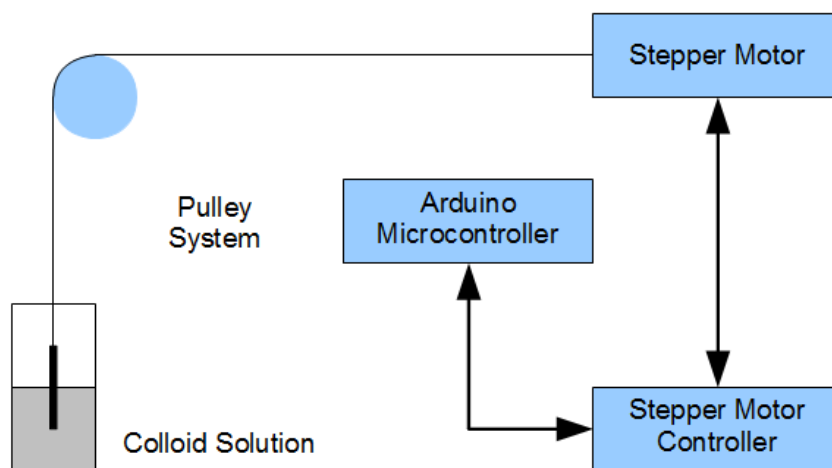


Figure 5.1 – Highly simplified schematics of the dip coating apparatus

The dip-coating assembly advances the step motor one step at a time by triggering relays connected to the step motor controller. The relays are controlled by an Arduino microcontroller, which is easily programmed to vary the period between subsequent steps of the step motor. The program for the microcontroller is documented in the Appendix. Each step that the step motor is advanced by the microcontroller pulls the substrate out of the colloid via the pulley system approximately 8  $\mu\text{m}$ .

Many different mixtures of solutions with varying amounts of each constituent were tested. The optimal solution composition is specified in Table 2.2.

<b>Material</b>	<b>% by Volume</b>
DI Water	65.0%
Methanol	21.6%
Silica Nanospheres	6.7%
Triton X-100	6.7%

Table 2.2 – Optimal Colloid Solution

Small deviations in the solution's composition changed the packing density of the monolayer drastically. However, the above solution is only optimized for use on glass and stainless steel substrates. Changing the substrate will, most likely, result in a different optimal solution.

Heating the colloid while dip-coating was also investigated. Heating the colloid to 50 °C, 75 °C, and 100 °C was found to have an increasingly negative impact on the packing density. Therefore, after sonicating the colloid to ensure complete dispersion prior to dip coating, the colloid was allowed to cool to room temperature. Further studies should be done to investigate dip-coating in an ice bath at low temperatures.

Varying the period of time between each advance of the step motor was also an important design parameter. Figure 2.2 shows SEM images using varying periods between advances in the step motor.

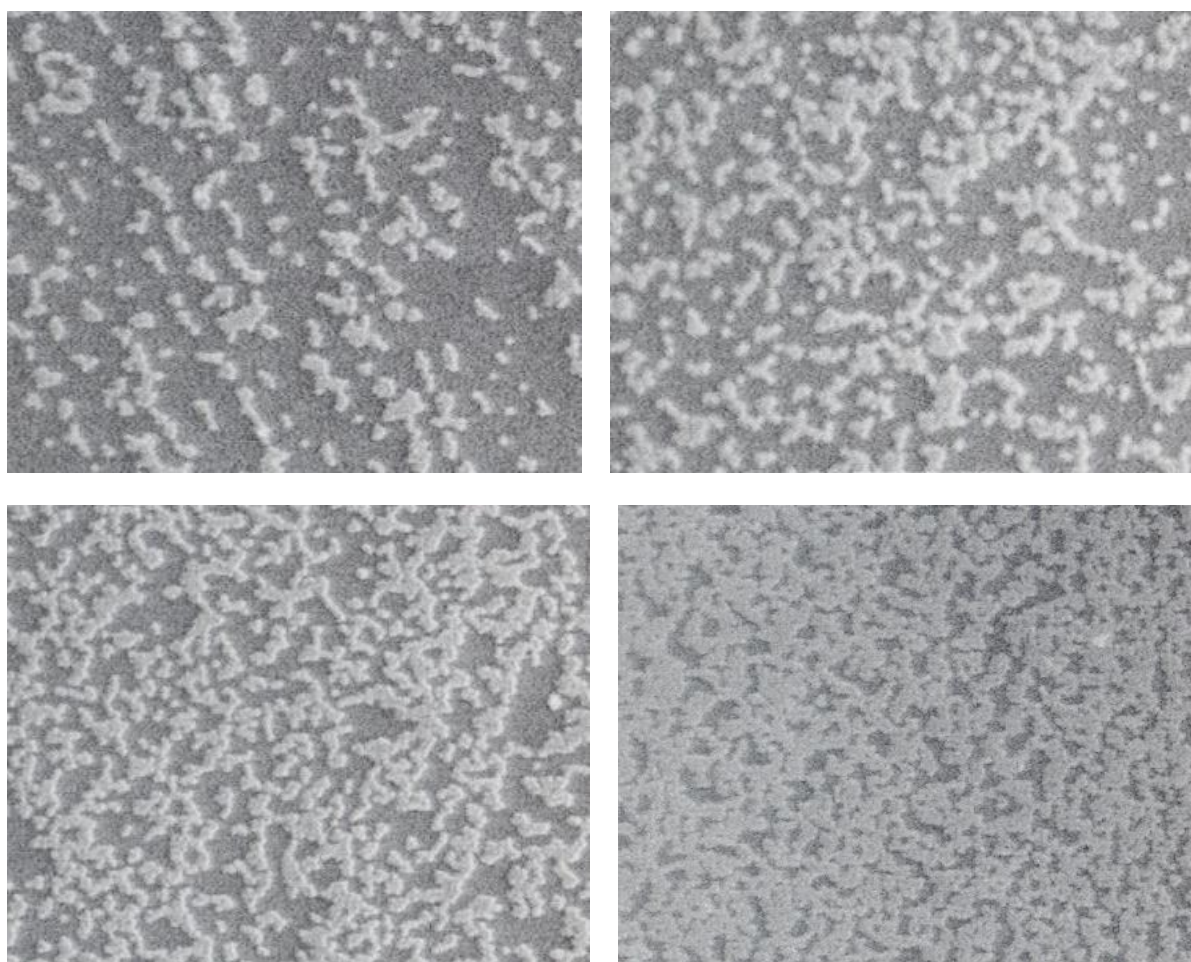


Figure 2.2 – SEM images showing 500nm nanospheres dip-coated at periods of 50ms, 100ms, 200ms, and 400ms between step motor advances from top left to bottom right.

It is clear that longer periods between the step motor advances result in to better packing densities. However, there is a limit at which the increases do not improve the packing densities; this limit is at ~600-800 milliseconds between step motor advances. In this research a constant periods of 800 milliseconds was therefore used.

Only half of the substrate was covered with  $\text{SiO}_2$  nanospheres so that the other half could be used as a reference when characterizing the cell.

### 2.1.4 Substrate Anneal

To ensure that the colloid solution has completely evaporated before depositing Ag on top of the nanospheres, a high temperature anneal was performed after dip-coating the substrates. The anneal was done at 500°C for 30 minutes. If some of the solution remained, the Ag layer would not adhere properly and flake off at a later time.

### 2.1.5 Ag Deposition

After the silica spheres were deposited across the substrate via the described dip-coating method, Ag was deposited on top of the spheres to create a highly reflective surface conforming to the texture of the spheres. Ag was chosen because of its highly reflective properties across the entire sunlight spectrum. Aluminum could be used, but it has slightly less reflective properties across all important wavelengths. Ag also makes a very highly conductive back contact as its sheet resistance is very low. The Ag was deposited using a custom-made thermal evaporator, by evaporating high purity Ag beads placed in a tungsten boat.

The evaporator was first cleaned and the substrates were loaded on a substrate holder approximately 18 inches away from the tungsten boat. The tungsten boat was then loaded with enough silver beads to ensure the entire evaporation could be done at once. The chamber was then evacuated to create a very high vacuum. Once the pressure in the chamber was below  $\sim 7 \times 10^{-7}$  Torr, the tungsten boat was heated by passing current through it. The tungsten boat and Ag were then put through a degas procedure to evaporate other contaminants from the Ag beads. During the degas procedure a shutter protected the substrates from the evaporating contaminants. After the degassing was

complete, the current was increased to ~1.9 Amps and the evaporation on the substrates was started by moving the shutter. The Ag evaporation rate was held constant at 0.4-0.5 nm/sec. This was done for an Ag layer thickness of 200 nm. The thickness of the Ag layer and deposition rate were monitored by a Maxtek TM200R thickness monitor.

### 2.1.6 ZnO:Al Deposition

ZnO:Al was deposited on top of the Ag layer to prevent agglomeration and eventual peeling of the Ag layer. Agglomeration of the Ag layer occurs when thin Ag films are deposited on a textured surface and introduced to a high-temperature environment. The Ag fills in the voids and creates a smoother surface in a lower energy configuration. The agglomeration effect is accelerated by the presence of Oxygen [20]. However, the ZnO:Al layer does reduce reflection of the silver layer as it absorbs some light as shown later in the Results and Discussion section.

The ZnO:Al was deposited in a rf sputtering system using a ZnO:Al target. The substrate was loaded into the chamber and the chamber was evacuated to create a very high vacuum. After allowing adequate time for the chamber to reach a sufficiently low pressure ( $<1 \times 10^{-6}$  Torr), the substrate heater was turned on. It is important to wait for a low pressure before turning on the substrate heater, as the presence of oxygen in the system from a less than adequately low pressure and heat will cause the substrate to oxidize and agglomerate. After the substrate has reached the proper temperature and the pressure is below  $1 \times 10^{-6}$  Torr, the deposition is ready to begin.

With a shutter between the target and substrate, argon gas was allowed to flow into the chamber. With all vacuum pump systems disconnected, the pressure was

allowed to rise to accommodate lighting a plasma by engaging the RF power supply. The turbo gate valve was then adjusted to bring the chamber to the deposition pressure. After a 2 minute stabilization period, the shutter was removed and the ZnO:Al was allowed to begin depositing on the substrate. A 200nm layer of ZnO:Al was deposited on the substrate before closing the shutter to stop the deposition process. The 200nm thickness was determined by careful calibration of the film. The ZnO:Al deposition parameters are shown in Table 2.3.

Deposition Pressure	100% Argon Flowmeter	RF Power	Deposition Temperature	Deposition Time
10 mTorr	20 sccm	30 Watt	150C	43.3 min

Table 2.3 – ZnO:Al Deposition Parameters

## 2.2 Solar Cell Deposition

As the substrates are completely made at this point, with layers of SiO<sub>2</sub> nanospheres, Ag, and ZnO:Al already deposited on the stainless steel substrate, the last step in the process is fabrication of a solar cell on the substrate.

### 2.2.1 a-si:H Cell Fabrication

The a-si:H deposition is done within a PECVD system. Each of the different layers of the a-si:H solar cell can be deposited using PECVD. PECVD depositions occur by introducing precursor gases into the plasma that is created between an electrode and the substrate holder. The precursor gases contain elements that are used to form the different layers. Silane (SiH<sub>4</sub>) is used as a precursor gas to form the intrinsic Si layer. Phosphine (PH<sub>3</sub>) is added to silane to form the n-type layers, diborane (B<sub>2</sub>H<sub>6</sub>) is added to

silane to form the p-type layers, and methane ( $\text{CH}_4$ ) is added to silane to form the Si carbide layers. A diagram showing a PECVD reactor is shown in Figure 2.3 [21].

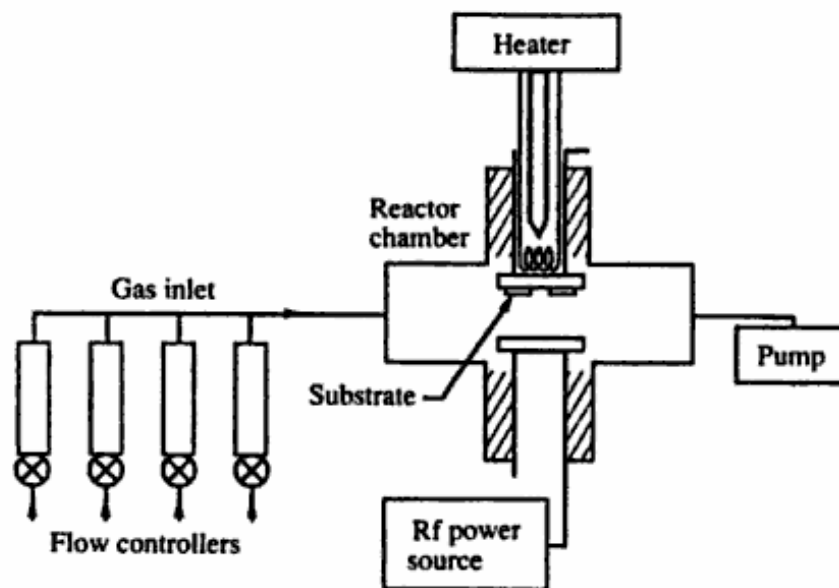


Figure 2.3 – Simplified schematic of a PECVD Reactor

The solar cell was deposited in a custom made PECVD reactor designed very closely to the one shown in Figure 2.3. The PECVD reactor used had a vertical substrate holder that held the substrate perpendicular to the ground, unlike in the holder shown in the figure.

To start the deposition process, the chamber was first evacuated by a pumping system. The pumping system, consisting of a mechanical roughing pump and a turbo-molecular pump backed with another mechanical pump, evacuated the system to a pressure below  $5 \times 10^{-7}$  Torr. This was done to eliminate any contaminants that could lead to defects in the solar cell. The substrate heater was then turned on and set to  $300^\circ\text{C}$ . After the substrate was at the proper temperature, the precursor gases for the n-type silicon carbide layer were allowed to flow and the RF signal was applied to the

electrodes to form the plasma. After the plasma was stabilized, the shutter was retracted and the deposition commenced. A thickness of 600nm was chosen to prevent shorts that occurred in a previous sample with an n-type silicon carbide layer thickness of 300nm. For the intrinsic layer, the process was repeated with only silane flowing as a precursor gas. The intrinsic layer was chosen to be between 250 and 300nm. The p-type Si layer was deposited following the intrinsic layer and was chosen to be approximately 25nm thick to allow for almost all of the incoming photons to pass through it and be absorbed by the intrinsic layer. Between the depositions of each layer, the RF power was disabled and the gasses were allowed to purge from the gas lines as to not induce unwanted doping in each of the other layers. It is important to note that each of the layers was previously calibrated for deposition rate to allow for precise thicknesses to be chosen.

### 2.2.3 ITO Deposition

After deposition of the a-si:H layers via PECVD, a top contact was made using the same sputtering system as described for ZnO:Al deposition. Differences in the deposition process were that a DC bias across the electrodes instead of a RF bias was used, a ITO target was used instead of a ZnO:Al target, and the gas flows into the chamber were different as well as the deposition conditions. A thickness of 70nm was chosen for the ITO layer as it optimizes losses from absorption and resistivity. A summary of the deposition parameters is shown in Table 2.4.

Deposition Pressure	100% Argon Flowmeter	1%/99% O <sub>2</sub> /Argon Flowmeter	DC Power	Deposition Temperature	Deposition Time
5 mTorr	16 sccm	4 sccm	20 Watt	225°C	3.5 min

Table 2.4 – ITO Deposition Parameters

## CHAPTER 3. CHARACTERIZATION

After the entire solar cell has been fabricated, each device was tested in various ways to determine the quality and unique characteristics of the cells. This was done using a variety of apparatus and techniques, which will be outlined in this section.

### 3.1 Substrate Characterization

The SiO<sub>2</sub> nanosphere texturing and packing density, along with the reflection properties of the finished substrate are important characteristics that were measured, both qualitatively and quantitatively throughout the development of the monolayer producing process. As mentioned, much of the research on the development of the process was done on 1” by 3” pre-cleaned microscope glass slides. This was due to their availability and size. Once the process was more refined, research was shifted towards using stainless steel substrates.

#### 3.1.1 Scanning Electron Microscopy (SEM)

Much of the characterization done on the substrate was done by texturing the substrate, annealing it as described, depositing a thin conductive layer of gold using a Hummer IV system, and inspecting the texture of the spheres in a JOEL-6100 SEM. A layer of gold was necessary to enable SEM imaging on the highly insulating surface of the SiO<sub>2</sub> nanospheres. The SEM system was also connected to a PC through the NPGS software package. This allowed for digital images to be saved for further inspection.

The use of the SEM was key in the early stages of the research. It is very difficult to determine packing density and quality of the monolayer of nanospheres. Many samples were discarded directly after being inspected under the SEM due to undesirable results.

### 3.1.2 Spectroscopy Measurements

If the nanosphere-coated sample was successful enough as determined from the SEM image, the Ag and ZnO:Al layers were deposited on it and spectroscopy measurements were performed. Diffuse and total reflection measurements were conducted on the samples to determine the overall properties of the back-reflector. These properties essentially determine how well the substrate was going to increase absorption for different wavelengths.

The spectroscopy measurement apparatus consisted of an Ocean Optics HR4000 spectrometer and an ISP-REF integrating sphere. This system used a tungsten-halogen light directed down a fiber-optic cable towards the sample. The light reflected off the sample is directed back down the fiber-optic cable and collected by the detector. Due to the detector and light source used, readings between 400-1000nm were considered valid. This apparatus allowed for total reflection (diffuse and spectral reflection combined) and diffuse reflection measurements. The integrating sphere used in the apparatus was Spectralon coated with > 98% diffuse reflectance for all wavelengths measured [22].

## 3.2 Solar Cell Device Characterization

After fabrication of the solar cells on the substrates, different measurements to determine their performance were made. These measurements are typical solar cell performance standards such as current density, open-circuit voltage, fill-factor, quantum efficiency, and efficiency.

### 3.2.1 I-V Measurement

I-V measurements were done using a custom apparatus that uses an ELH bulb as a light source calibrated for AM1.5 intensity. The solar cell was placed underneath the light source at the point of AM1.5 intensity. Small probes were put on the ITO top contact and the Ag back contact. A sweep of voltages was then applied across the probes and the current measured. From these measurements, a graph, like that in Figure 3.1, can be made: it can be visually inspected to determine many important characteristics of the solar cell.

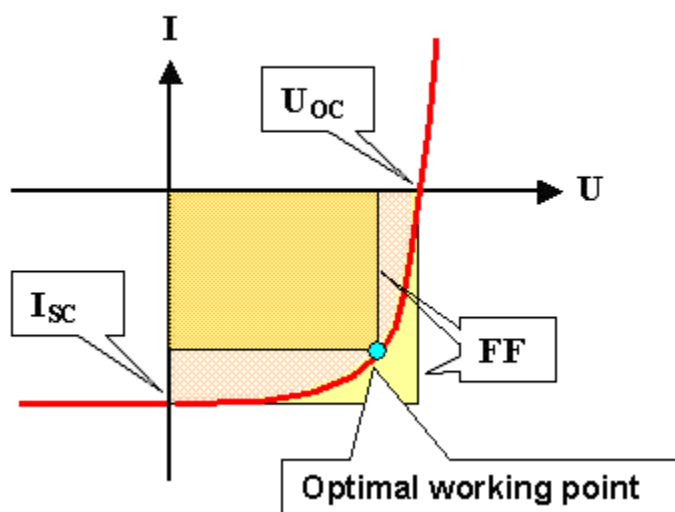


Figure 6.1 – Sample IV Curve of a Solar Cell

The open circuit voltage ( $U_{oc}$  or  $V_{oc}$ ), the short circuit current ( $I_{sc}$ ), the area being tested ( $A$ ) and the fill factor ( $FF$ ) alone can show the efficiency when measured under AM1.5 conditions using Equation 3.1, where  $100\text{mW}/\text{cm}^2$  is the power density of the AM1.5 spectrum.

$$\eta = \frac{I_{sc} * V_{oc} * FF}{A * 100\text{mW}/\text{cm}^2} \quad (3.1)$$

Fill factor is a measure of the amount of photons absorbed divided by the losses due to series resistance and shunt resistance and can be calculated by using the voltage ( $V_{maxP}$ ) and current ( $I_{maxP}$ ) at the point of maximum power (optimal working point) using Equation 3.2.

$$FF = \frac{I_{maxP} * V_{maxP}}{I_{sc} * V_{oc}} \quad (3.2)$$

Series resistance is a measure of the resistance of the contacts and is calculated from the slope of the I-V curve at and around  $V_{oc}$ . Low shunt resistance is due to material defects and interface issues and is measured from the slope of the I-V curve around  $I_{sc}$ . A high shunt resistance and a low series resistance are desirable qualities and lead to a high fill factor.

### 3.2.3 Quantum Efficiency Measurement

One of the most important measurements in solar cell characterization is quantum efficiency. Quantum efficiency explains how efficient a solar cell is at absorbing photons and converting them into current at a given wavelength. One can also use a quantum efficiency measurement to obtain the current density,  $J_{sc}$  using equation 3.3.

The quantum efficiency apparatus, shown in Figure 3.2, consists of a light source combined with monochromator using a chopper wheel, the light is chopped at a frequency of 13 Hz. The light then travels through a series of lenses and filters, filtering out any harmonic multiples of the base wavelength. The light is then directed down at the sample, focused on the ITO at a minimal beam width.

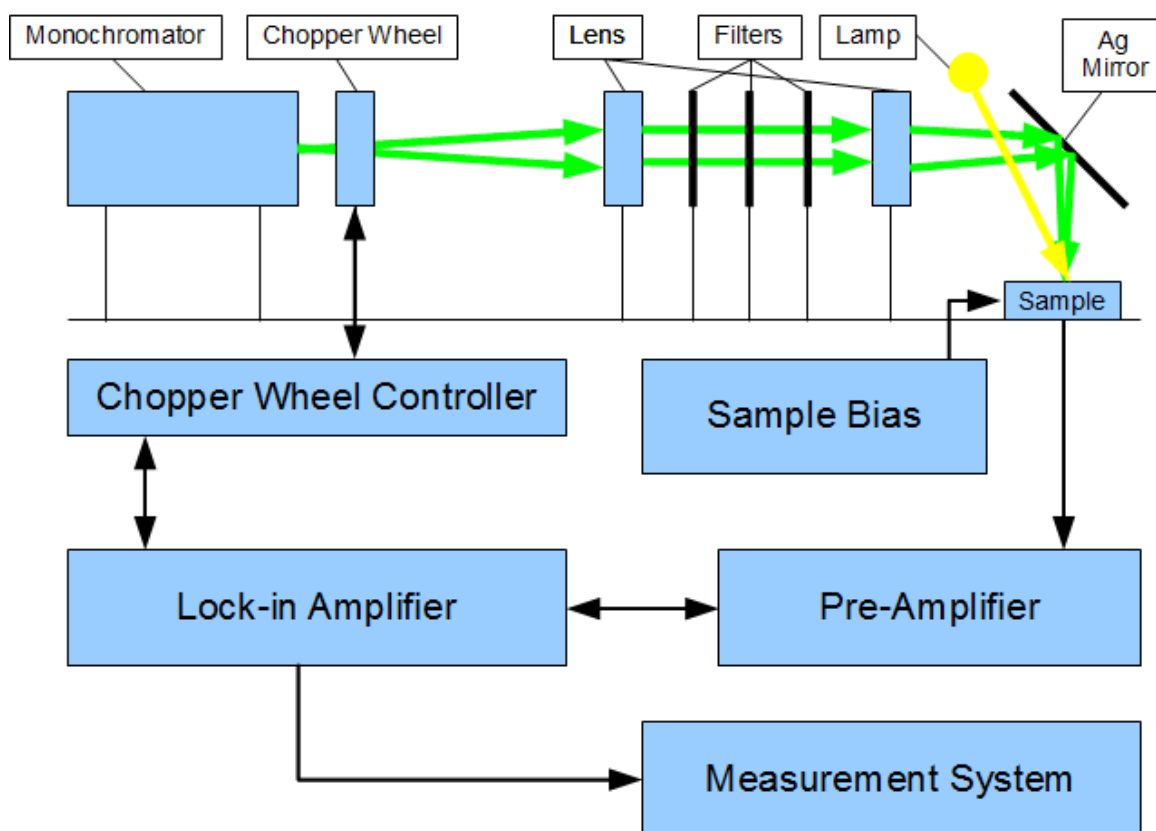


Figure 3.2 – Diagram of the Quantum Efficiency Measurement System

A bias lamp is also directed at the sample at near AM1.5 intensity to fill the trap states and ensure that the real quantum efficiency is being measured. The voltage across the sample is controlled by a voltage source labeled Sample Bias in the figure. Since the voltage is held constant, the current is measured and sent through a current pre-amplifier. The current pre-amplifier amplifies the current and converts it into a voltage

to be read by the lock-in amplifier. As the light is being chopped at a frequency of 13 Hz, the lock-in amplifier receives a signal from the chopper wheel controller and matches it with the signal coming from the pre-amplifier. This signal is then read to a measurement system. As the voltage being read is directly related to the current coming from the solar cell, the voltage is also directly related to the number of photons absorbed and collected from the solar cell. The voltage response was measured for 0V and 0.5V sample bias at wavelengths from 400nm to 800nm in 10nm increments. The voltage response was also measured for a reference cell of known quantum efficiency. All this information is applied in Equation 3.4 to calculate external quantum efficiency (EQE).

$$EQE = QE_{reference\ cell} * \frac{V_{sample}/A_{sample}}{V_{reference}/A_{reference}} \quad (3.4)$$

Because the sample and the reference area illuminated by the monochromatic light are unknown, we use Equation 3.5 and normalize the quantum efficiency so that it equals 90% at its peak quantum efficiency to obtain the normalized quantum efficiency

$$EQE_{normalized} = QE_{reference\ cell} * \frac{V_{sample}}{V_{reference}} \quad (3.5)$$

## CHAPTER 4. RESULTS AND DISCUSSION

### 4.1 Nanosphere Substrates

#### 4.1.1 Dip-Coating Apparatus

Much of the research done was on the formulation of a monolayer by a dip-coating method. The initial design of the dip-coating apparatus was very crude. The apparatus pulled the sample out of the colloid at a very uneven rate. The final design was more complicated, involving a step-motor advancing a pulley system with a mechanical advantage approximately equal to 10. The final design allowed for more repeatable results and a much slower pulling rate. However, it was not without flaws. Due to friction in various parts and an undampened system, the dip-coater pulled the samples out in a periodically uneven rate. The uneven rate caused areas of densely packed spheres as well as areas of sparsely packed spheres. Discontinuities in the sphere packing density can be seen perpendicular to the pulling direction in Figure 4.1.

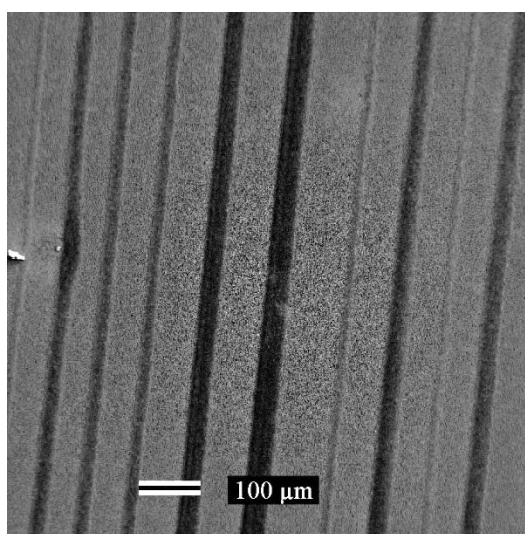


Figure 7.1 – Periodic bunching of monolayer due to imperfections in the dip-coating apparatus

When inspected at a higher magnification, the effects can range from a narrow line of incoherence to a region void of nanospheres as in Figure 4.2, depending on the colloid solution and pulling speed.

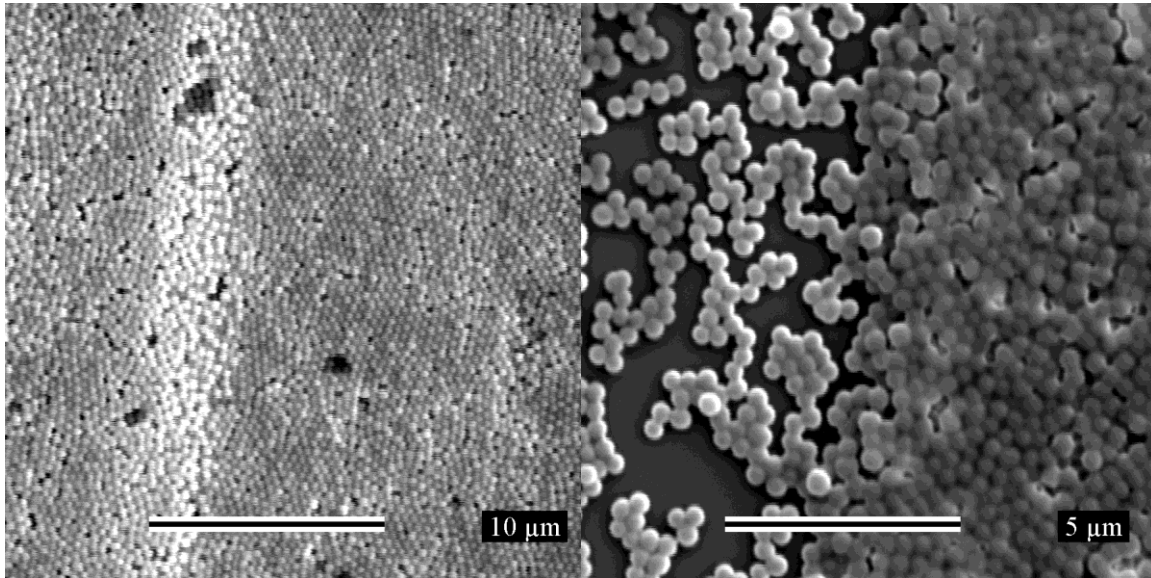


Figure 4.2 – High magnification of periodic bunching

Even though these problems were designed to be minimized by careful manipulation of the colloid solution, their effects were never completely eliminated. Visual inspection of the substrates and finished solar cells shows parallel lines corresponding to the period bunching.

#### 4.1.2 Colloid Composition

Use of the proper colloid, as defined in Table 2.2, was essential in producing an effective monolayer. The colloid used in this research was found to work equally well when deposited on glass or stainless steel, two popular solar cell substrates. It is very likely that this colloid can be deposited on more substrates to form monolayers for other

research opportunities. Figure 4.3 shows an SEM image of a monolayer of nanosphere particles on a glass substrate compared to one on a stainless steel substrate.

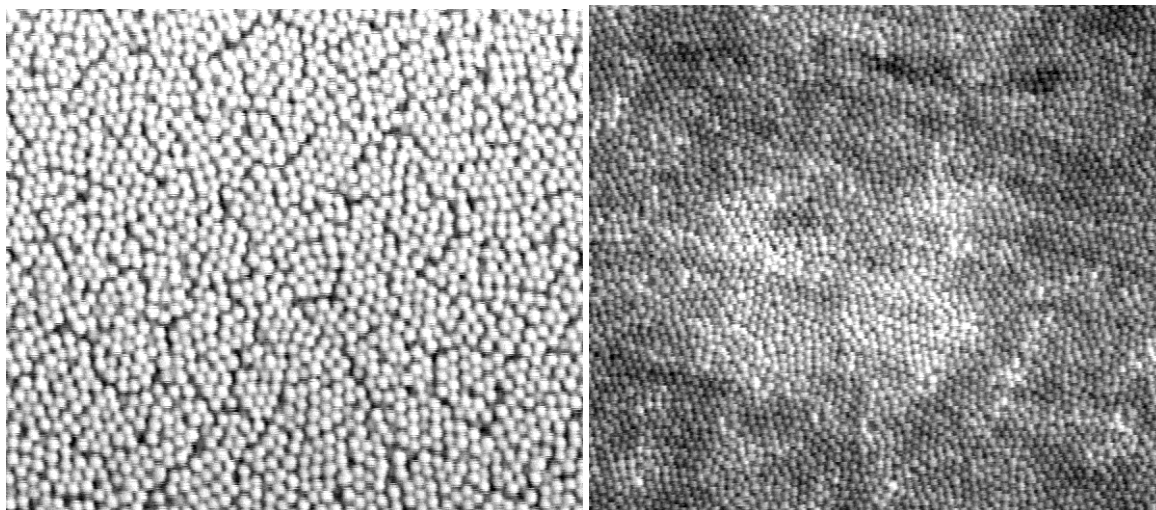


Figure 4.3 – Monolayer of nanosphere particles deposited on glass (left) and stainless steel (right) with a layer of Ag deposited on top of the nanospheres

### 4.1.3 Substrate Characteristics

After 200nm of Ag was deposited on both a flat stainless steel substrate as well as a stainless steel substrate with a nanosphere monolayer deposited on it, diffuse reflection measurements were taken. Figure 4.4 shows increased diffuse reflection of the nanosphere textured substrate labeled by SiO<sub>2</sub> (as it is for the rest of the measurements) over the flat substrate labeled by Flat. Measurements shown in Figure 4.4 are for the substrates both having only the 200nm Ag deposited on them. Figure 4.5 shows the diffuse reflection of each substrate after 200nm ZnO:Al had been deposited on the Ag as well as the substrates. Maximal diffuse reflection has been shown to occur at packing densities much lower than 100% [24], but a monolayer was desired in this research.

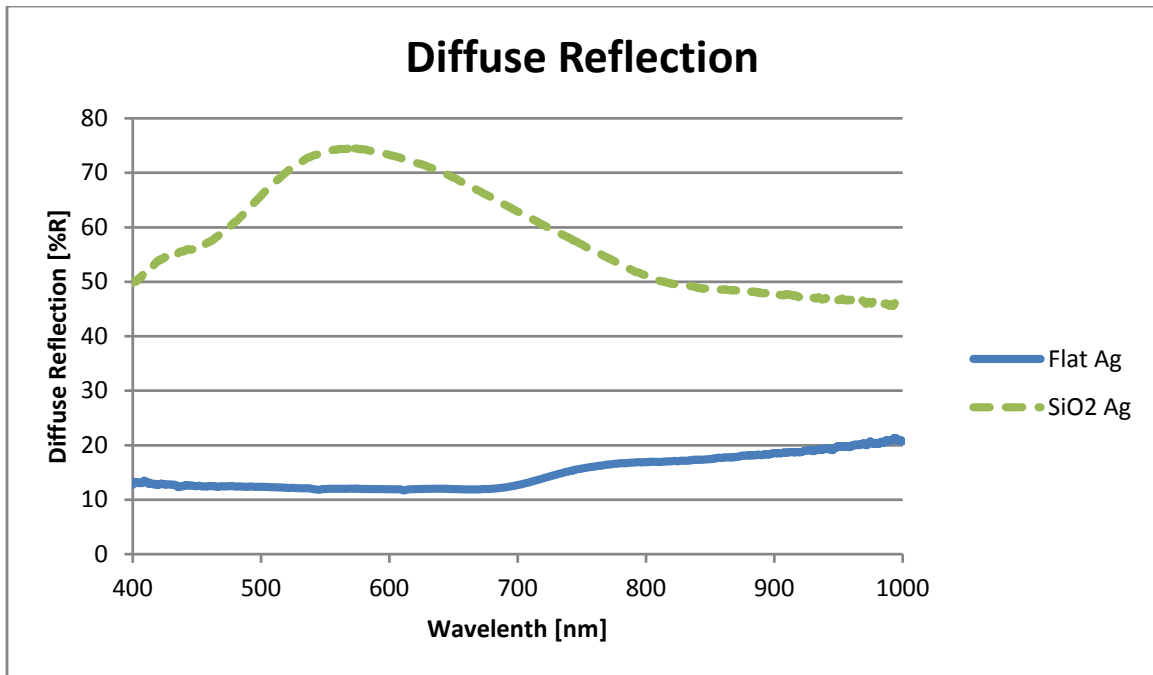


Figure 4.4 – Diffuse reflection of substrates after Ag deposition

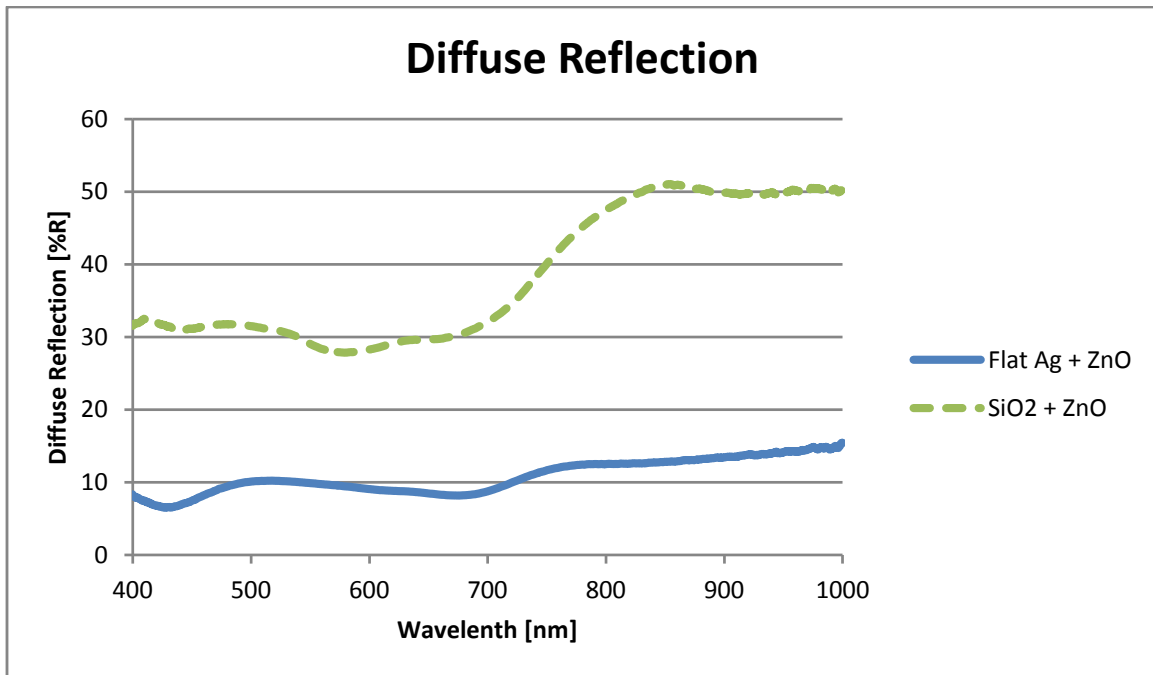


Figure 4.5 – Diffuse reflection of substrates after ZnO:Al deposition

Use of thinner ZnO:Al would have facilitated a higher diffuse reflection for the nanosphere substrate, but a thicker layer was initially chosen to minimize device shorts due to large voids in the nanosphere texture. Figure 4.6 shows the total reflection of the substrates. Clearly, the nanosphere substrate has a lower total reflection, which suggests that a thicker layer of Ag could be used in later research to increase total reflection.

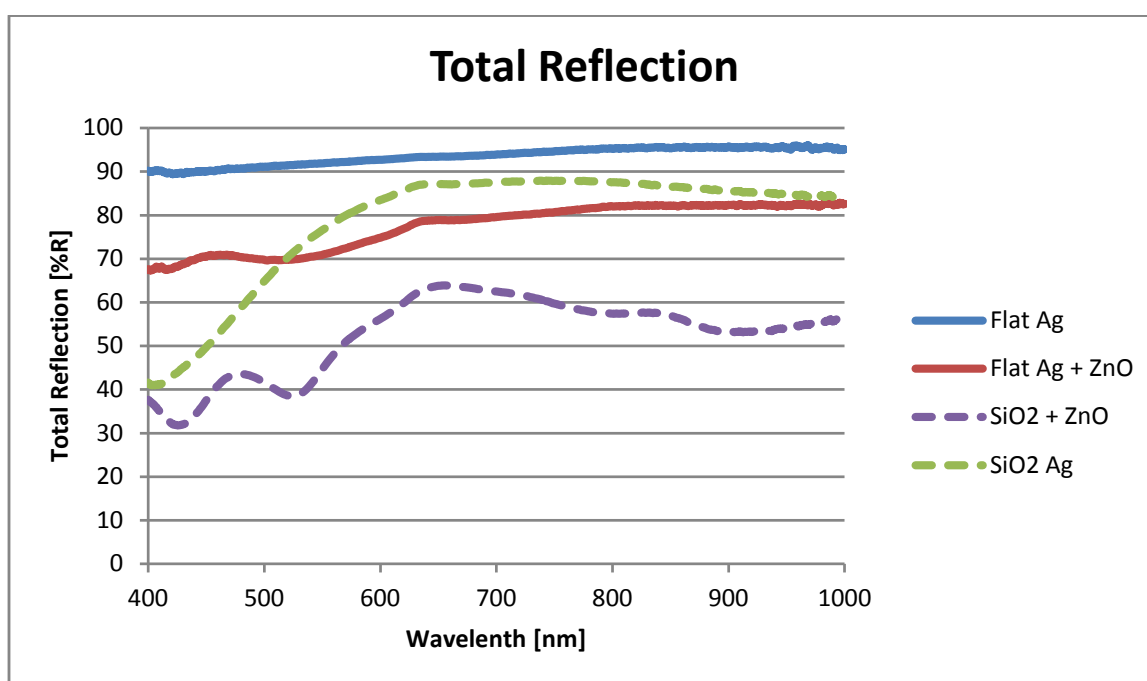


Figure 4.6 – Total reflection of substrates after Ag and ZnO:Al depositions

## 4.2 Solar Cell Devices

### 4.2.1 a-Si:H Devices

Two successful n-i-p a-Si:H devices were fabricated on stainless steel substrates that had a nanosphere textured substrate on half and a flat surface on the other half. The first device made failed due to shorts caused by an inadequate thickness of the n-type

layer. Therefore, the n-type layer thickness was increased from 300nm to 600nm for the two successful devices, the best which will be extensively characterized. As previously mentioned, half of the substrate was left un-textured and had only the 200nm Ag and 200nm ZnO:Al deposited on the surface. This was done to provide a flat, non-textured reference for the nanosphere textured solar cells. After the solar cell was fabricated, a SEM image of the p-type surface was taken, seen in Figure 4.7. It can be seen that the a-Si:H cell grew conformally on the surface of the nanosphere textured substrate, revealing a similar texture on the top surface of the solar cell.

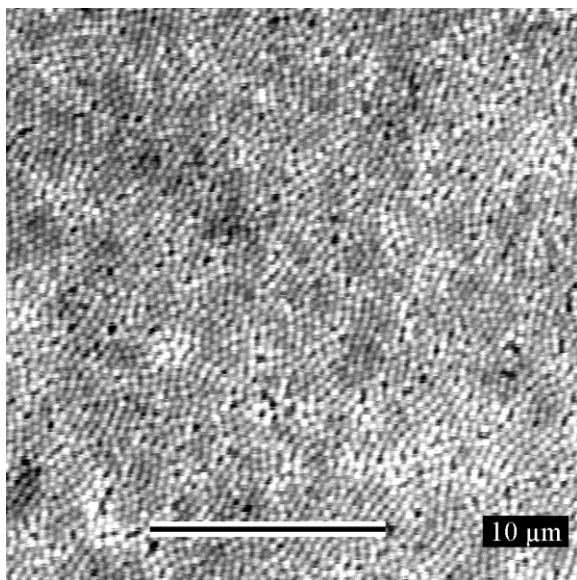


Figure 4.7 – SEM image of the top surface of the solar cell device

A summary of the device characteristics obtained by fully characterizing the solar cells fabricated is shown in Table 4.1. The summary is divided by back reflector type (SiO<sub>2</sub> nanosphere or flat) and device number.

Type	Device	$V_{oc}$ [V]	$I_{sc}$ [mA]	FF	Series Resistance [ohms]	Shunt Resistance [ohms]	$J_{sc}$ calculated from QE [mA/cm <sup>2</sup> ]
SiO <sub>2</sub>	2-13182	0.886	1.52	46.9	222	4450	12.52
Flat	2-13182	0.896	1.35	66.4	72.8	13800	11.79
SiO <sub>2</sub>	2-13187	0.89	1.48	42.1	274	3190	12.62
Flat	2-13187	0.919	1.39	66	79.4	12900	11.95

Table 4.1 – Summary of device characteristics

The summary shows a clear increase in short circuit current ( $I_{sc}$ ), taken from the IV measurement as well as the current density ( $J_{sc}$ ), calculated from the EQE measurement. An average increase of 9.5% in  $I_{sc}$  and 5.9% in  $J_{sc}$  for the nanosphere substrate shows an increase in carrier collection and subsequently an increase in overall absorption across the entire solar spectrum. Inspecting Figure 4.8 reveals a large increase in normalized EQE for the nanosphere substrate, most noticeably at the longer wavelengths where absorption is normally low. This agrees with the earlier conclusion of increased absorption for the nanosphere substrates from inspection of the IV data. This increase in absorption is due to the higher diffuse reflection at long wavelengths where normal thin-film solar cells are unable to efficiently absorb photons due to the low absorption coefficient requiring a long path length for effective absorption.

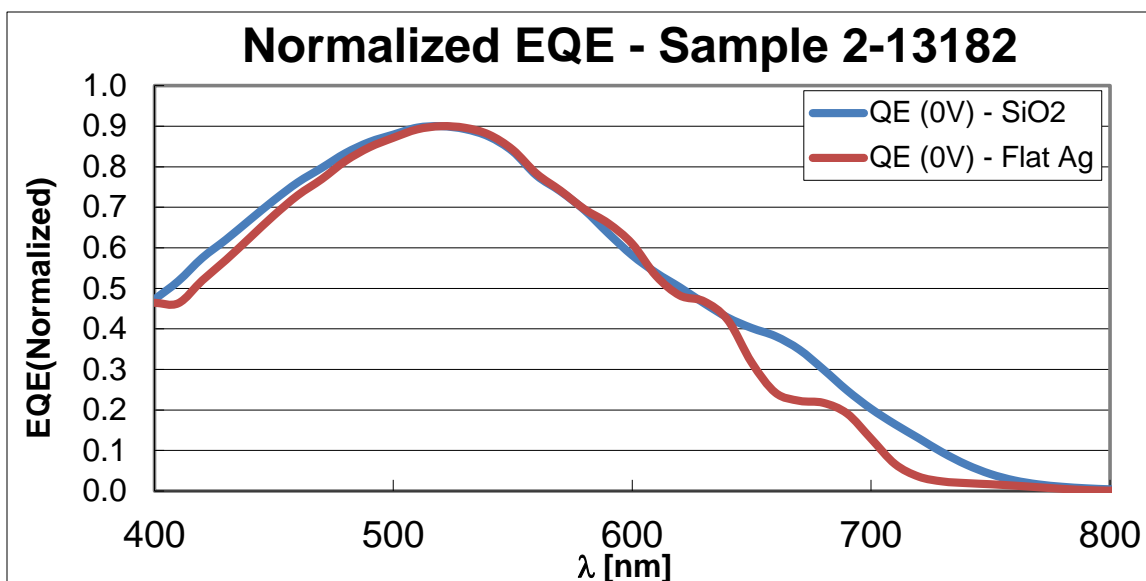


Figure 4.8 – Normalized EQE measurement of sample 2-13182

Further evidence showing absorption enhancement is shown in Figure 4.9 where the ratio of normalized EQE for the nanosphere textured substrate versus the flat substrate is plotted as EQE enhancement; as the wavelengths get longer, the average EQE enhancement increases. This confirms an increase in absorption for long wavelengths.

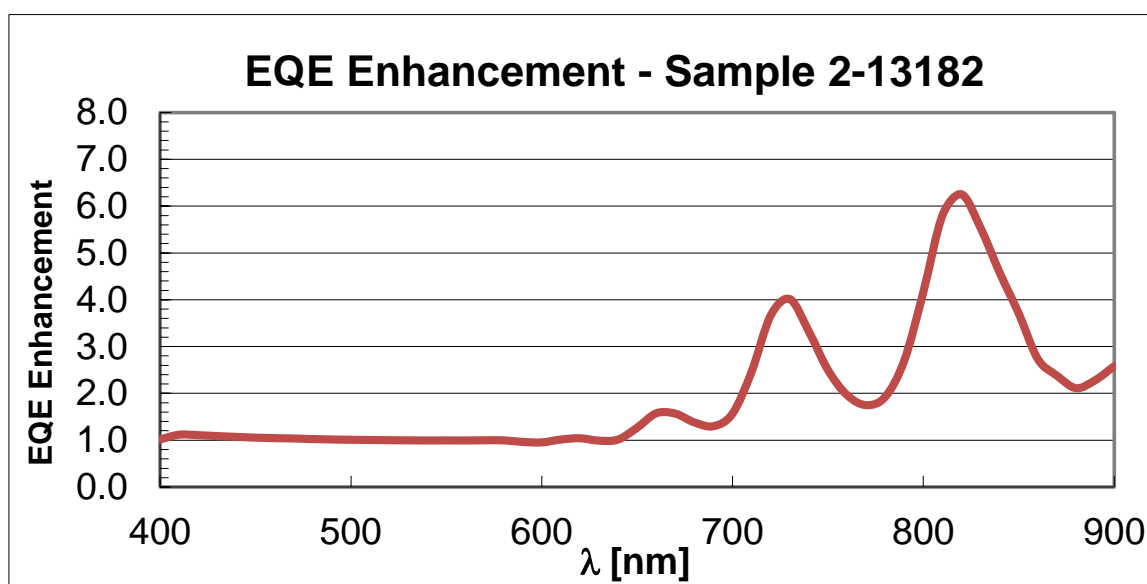


Figure 4.9 – EQE enhancement of sample 2-13182

The nanosphere substrate devices did suffer a large increase in series resistance as well as a decrease in shunt resistance when compared to the flat reference. This detracts from the fill factor as well as the overall efficiency and is seen visually in Figure 4.10.

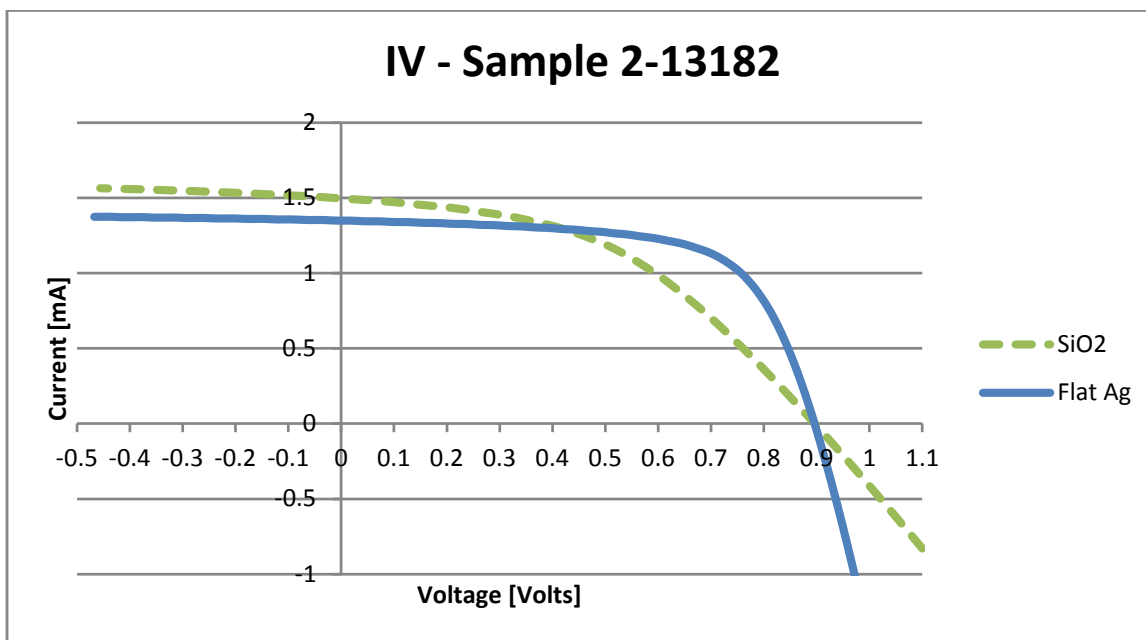


Figure 4.10 – IV measurement of sample 2-13182

### 4.2.2 nc-Si:H Devices

While nc-Si:H devices were attempted, the increased strain in the nanocrystalline material combined with the weakness of the nanosphere texture at the periodic bunching interfaces destructively combined. All devices fabricated quickly failed due to structures peeling and flaking off. This is illustrated in the SEM of a nc-Si:H device in Figure 4.11.

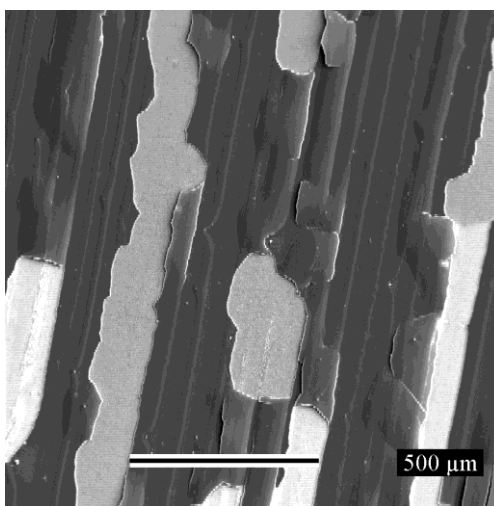


Figure 4.11 – SEM image of nc-Si:H device peeling off at periodic bunching boundaries

## CHAPTER 5. CONCLUSIONS AND FUTURE WORK

A method and apparatus for producing monolayers of silica nanospheres on stainless steel and glass substrates was developed. This method was used to produce a short-range ordered monolayer for use as a textured back-reflector when combined with a reflective metal layer. Modest increases of current density were seen, and an increase in long wavelength absorption was observed.

Future work to improve this method could be done by optimizing the thickness of the Ag and ZnO:Al layers for increased diffuse and total reflection. Other future work could involve using the dip-coating method at a lower step-motor period to optimize the packing density for diffuse reflection. This work combined with lower series resistance in the solar cell and a higher fill factor could prove to be a viable high-output, roll to roll processing technique for producing back-reflector texturing in thin-film solar cells.

The method for creating a monolayer could also be used improved by improving the apparatus to eliminate the periodic “jerking” and allow for a lower pulling rate. This would allow for better, more periodic monolayers that could be used for other research applications such as the fabrication of nanorods, nanocones, and nanodots.

## APPENDIX: DIP-COATER ARDUINO CODE

```
// Puller Program
#include <LiquidCrystal.h>#include <LiquidCrystal.h>

int pullEastPin = 8;
int pullWestPin = 9;
int triggerPin = 10;
int ledPin = 13;
int pulseDelayTime = 10;
LiquidCrystal lcd(7, 6, 5, 4, 3, 2);

// The setup() method runs once, when the sketch starts

void setup() {
  // initialize the digital pin as an output:
  pinMode(pullEastPin, OUTPUT);
  pinMode(pullWestPin, OUTPUT);
  pinMode(ledPin, OUTPUT);
  pinMode(triggerPin, INPUT);
  lcd.begin(16, 2);
  lcd.print("Puller Program");
  zahraMarquee(200);
}
void pull(int ticks, int delayTime)
{
  for (int i = 1; i<=ticks; i++)
  {
    lcd.clear();
    lcd.setCursor(0,0);
    lcd.print("Period: ");
    lcd.setCursor(8,0);
    lcd.print(delayTime);
    lcd.setCursor(0,1);
    lcd.print("Tick # ");
    lcd.setCursor(7,1);
    lcd.print(i);
    digitalWrite(pullWestPin, HIGH);
    digitalWrite(ledPin, HIGH);
    delay(pulseDelayTime);
  }
}
```

```
digitalWrite(pullWestPin, LOW);
digitalWrite(ledPin, LOW);
delay(delayTime - pulseDelayTime);
}
}
void loop()
{
  if (digitalRead(triggerPin) == HIGH)
  {
    // This is where to specify different pull periods and amount of step motor advances
    // Pull(8000, 800) means 8000 advances at a period of 800ms
    pull(8000, 800);
    delay(1000000000);
  }
}
```

## BIBLIOGRAPHY

- [1] BP. "BP Statistical Review of World Energy." June 2009.
- [2] "GE Invests, Delivers One of World's Largest Solar Power Plants,"  
<http://www.huliq.com/18313/ge-invests-delivers-one-of-worlds-largest-solar-power-plants>.
- [3] A. V. Shah et al., "Material and Solar Cell Research in Microcrystalline Silicon,"  
*Solar Energy Materials and Solar Cells*, Vol. 78, No. 1, P. 469–492, 2003.
- [4] B. Streetman and S. Banerjee, *Solid State Electronic Devices*, Edition. 5, 1999.
- [5] D. Jaworske, "Reflectivity of Silver and Silver-Coated Substrates From 25°C to 800°C," <http://ieeexplore.ieee.org/stamp/stamp.jsp?arnumber=00659223>
- [6] S. Pellicori, "Think Film Photovoltaic Solar Cells," *Coating Materials News*, Vol. 19, No. 4, December 2009.
- [7] D. K. Mynbaev, L. L. Scheiner, "Snells Law," *Fiber-Optic Communications Technology*, P. 35, 2001.
- [8] R. Swanepoel, "Determination of the Thickness and Optical Constants of Amorphous Silicon," *J. Phys. E: Sci. Instrum.*, Vol.16, May 1983.
- [9] T. Margalith, O. Buchinsky, D. A. Cohen, A. C. Abare, M. Hansen, S. P. DenBaars, and L. A. Coldren, "Indium Tin Oxide Contacts to Gallium Nitride Optoelectronic Devices," *Applied Physics Letters*, Vol. 74, No. 26, April 1999.
- [10] B. Rech, O. Kluth, T. Repmann, T. Roschek, J. Springer, J. Müller, F. Finger, H. Stiebig, and H. Wagner, "Solar Energy Mater," *Solar Cells*, Vol.74, P. 439, 2002.

- [11] J. Springer, "Absorption Loss at Nanorough Silver Back Reflector of Thin-Film Silicon Solar Cells," *Journal of Applied Physics*, Vol. 95, No. 3, 2004.
- [12] B. Curtin, R. Biswas, and V. Dalal, "Photonic Crystal Based Back Reflectors for Light Management and Enhanced Absorption in Amorphous Silicon Solar Cells," *Applied Physics Letters* 95, No. 231102, December 2009.
- [13] R. Biswas and D. Shou, "Simulation and Modelling of Photonic and Plasmonic Crystal Back Reflectors for Efficient Light Trapping," *Phys. Status Solidi A* 207, No. 3, P. 667-670, December 2009.
- [14] M. Fonrodona, "PEN as Substrate for New Solar Cell Technologies," *Solar Energy Materials and Solar Cells*, Vol. 89, No. 1, P. 37-47, October 2005.
- [15] T. Soderstrom, F. Haug, V. Terrazzoni-Daudrix, and C. Ballif, "Flexible Micromorph tandem a-Si/ $\mu$ c-Si Solar Cells," *Journal of Applied Physics*, Vol. 107, P. 014507, 2010.
- [16] J. Yang, B. Yan, G. Yue, S. Guha, "Light Trapping in Hydrogenated Amorphous and Nano-Crystalline Silicone Thin Film Solar Cells."
- [17] C. L. Cheung, R. J. Nikolic, C. E. Reinhardt and T. F. Wang, "Fabrication of Nanopillars by Nanosphere Lithography," *Nanotechnology*, Vol. 17, No. 5, March 2006.
- [18] S. Yang, S. G. Jang, D. Choi, S. Kim, and H. K. Yu, "Nanomachining by Colloidal Lithography," *Small Journal*, No. 4, P. 458-475, 2006.
- [19] "Angstrom Sphere, Uniform Micron-Sized Silica Spheres," *Product Datasheet*.
- [20] S. K. Sharma, and J. Spitz, "Hitlock Formation, Hole Growth and Agglomeration in Thin Silver Films," *Thin Solid Films*, Vol. 65, No. 3, P. 339-350, May 1979.

- [21] R. A. Street, "Hydrogenated Amorphous Silicon," *Cambridge Solid State Science Series*, P. 19, 1991.
- [22] "ISP-REF Integrating Sphere," <http://www.oceanoptics.com/products/ispref.asp>.
- [23] "Iv Solar Cell," [http://www.tf.uni-kiel.de/matwis/amat/semitech\\_en/kap\\_8/illustr/iv\\_solar\\_cell\\_simple.gif](http://www.tf.uni-kiel.de/matwis/amat/semitech_en/kap_8/illustr/iv_solar_cell_simple.gif).
- [24] R. Boesch, "SiO<sub>2</sub> nanosphere textured back reflectors for enhanced light trapping in amorphous and nanocrystalline silicon solar cells," Master's thesis, Iowa State University, 2009.
- [25] B. Curtin, "Photonic crystal back-reflectors for light management and enhanced absorption in a-Si:H solar cells," Master's thesis, Iowa State University, 2009.

## ACKNOWLEDGEMENTS

I would first like to thank Vikram Dalal. Without your support and guidance, I likely would have never entered research, the microelectronics field, or graduate school. I would also like to thank Rana Biswas for being my major professor and for letting me help on the photonic crystals project. Thanks must go to Joe and Ruth Shinar, for being on my committee, letting me help out with your projects, and providing great guidance and editing my papers (Ruth). I would like to thank Max Noack for being the glue that keeps the MRC running. Without your training and helpful support, I would have not succeeded. I would also like to thank Kay Han, Nayan Chakravarty, and Sambit Pattnaik for their help in device fabrication.

I would also like to acknowledge all of the MRC students and frequent visitors whom I've known over the years and become friends with: Ben Curtin, Michael Eggleston, Alex Smith, Sambit Pattnaik, Bob Mayer, Nayan Chakravarty, Atul Madhavan, Satya Saripalli, Emily Evers, Jason Jirak, and Aaron Thoeming. Thank you for the interesting conversations, intellectual support, and company at the 8AM meetings.

I must thank my roommates, whom have put up with me for the last five years: Kyle, Teff, Kendal, and Bill and for all of the all-nighters that we endured. I would like to thank Zahra for being supportive and helpful through it all. Last, but certainly not least, I would like to thank my family for their support and for checking up on me from time to time.